

# Responses of Shallow Cumulus Convection to Large-Scale Temperature and Moisture Perturbations: A Comparison of Large-Eddy Simulations and a Convective Parameterization Based on Stochastically Entraining Parcels

JI NIE

*Department of Earth and Planetary Sciences, Harvard University, Cambridge, Massachusetts*

ZHIMING KUANG

*Department of Earth and Planetary Sciences, and School of Engineering and Applied Sciences, Harvard University, Cambridge, Massachusetts*

(Manuscript received 17 October 2011, in final form 3 January 2012)

## ABSTRACT

Responses of shallow cumuli to large-scale temperature/moisture perturbations are examined through diagnostics of large-eddy simulations (LESs) of the undisturbed Barbados Oceanographic and Meteorological Experiment (BOMEX) case and a stochastic parcel model. The perturbations are added instantaneously and allowed to evolve freely afterward. The parcel model reproduces most of the changes in the LES-simulated cloudy updraft statistics in response to the perturbations. Analyses of parcel histories show that a positive temperature perturbation forms a buoyancy barrier, which preferentially eliminates parcels that start with lower equivalent potential temperature or have experienced heavy entrainment. Besides the amount of entrainment, the height at which parcels entrain is also important in determining their fate. Parcels entraining at higher altitudes are more likely to overcome the buoyancy barrier than those entraining at lower altitudes. Stochastic entrainment is key for the parcel model to reproduce the LES results. Responses to environmental moisture perturbations are quite small compared to those to temperature perturbations because changing environmental moisture is ineffective in modifying buoyancy in the BOMEX shallow cumulus case.

The second part of the paper further explores the feasibility of a stochastic parcel-based cumulus parameterization. Air parcels are released from the surface layer and temperature/moisture fluxes effected by the parcels are used to calculate heating/moistening tendencies due to both cumulus convection and boundary layer turbulence. Initial results show that this conceptually simple parameterization produces realistic convective tendencies and also reproduces the LES-simulated mean and variance of cloudy updraft properties, as well as the response of convection to temperature/moisture perturbations.

## 1. Introduction

Shallow cumulus convection plays important roles in the large-scale atmospheric circulation. By enhancing vertical transport of heat and moisture, shallow cumuli regulate the surface fluxes and maintain the thermodynamic structures over the vast subtropical trade wind region, a region that also provides the inflow for the deep convective intertropical convergence zone. It has long been recognized that representations of shallow cumulus convection in large-scale models significantly

impact the resulting circulation (e.g., Tiedtke 1989). More recently, it has been further suggested that, because of its abundance, the shallow cumuli are a leading factor in determining the cloud–climate feedback (Bony et al. 2004; Bony and Dufresne 2005). It is therefore important to understand the dynamics of shallow cumulus convection and to better parameterize it in global climate models or general circulation models (GCMs).

Our strategy to better understand shallow cumuli is to look at how they respond to small perturbations to their large-scale environment. This approach has been applied previously to deep convection (Mapes 2004; Kuang 2010; Tulich and Mapes 2010; Raymond and Herman 2011). Kuang (2010) was able to determine the responses of convection (using a cloud system-resolving

---

*Corresponding author address:* Ji Nie, Department of Earth and Planetary Sciences, Harvard University, Cambridge, MA 02138.  
E-mail: jinie@fas.harvard.edu

model) to a sufficiently complete set of perturbations in their large-scale environment and to use these responses to approximate the behavior of convection near a reference state. A range of interesting behaviors was found, such as stronger sensitivity of convection to temperature perturbations in the lower troposphere than those in the upper troposphere (Kuang 2010; Tulich and Mapes 2010; Raymond and Herman 2011). The physical processes behind the responses, however, are not yet fully understood (Kuang 2010; Tulich and Mapes 2010). In this study, we shall use shallow nonprecipitating convection, the dynamics of which are simpler without the many complicating processes associated with precipitation, as a starting point to understand and model the physical processes behind the responses of cumulus convection to large-scale temperature and moisture perturbations.

Despite its relative simplicity, shallow cumulus convection involves interactions among a number of subcomponents, such as the subcloud layer, whose thermodynamic properties and turbulence statistics, together with the strength of convective inhibition, set the properties and the amount of cloudy updrafts at the cloud base; the interactions between clouds and their environment and within the clouds themselves, which determine the evolution of cloudy updrafts as they rise from the cloud base; and the fate of these cloudy updrafts as they penetrate into the inversion layer. These interactions are reflected in the construct of many contemporary parameterizations (e.g., Bretherton et al. 2004; Neggers and Siebesma 2002). In this paper, we will focus on perturbations in the cloud layer (above the cloud base but below the inversion), thus emphasizing the evolution of cloudy updrafts as they rise from the cloud base. Being able to better study individual processes in isolation is an advantage of looking at responses to small perturbations, as the other subcomponents can be regarded as mostly unchanged.

In addition to how heating and moistening rates averaged over the whole cumulus ensemble change in response to temperature and moisture perturbations, we place special emphasis on changes in the statistical distributions of cloudy updrafts. While many of the current shallow schemes are bulk schemes (e.g., Kain and Fritsch 1990; Bretherton et al. 2004), it is important to capture the statistical distribution of the cloudy updrafts in order to better simulate microphysics and chemistry beyond the goal of simulating heating and moistening tendencies. This is similar to efforts of probability distribution function (PDF)-based parameterizations (e.g., Lappen and Randall 2001; Larson et al. 2002; Golaz et al. 2002).

This paper has two parts. In the first half, we aim to understand changes in the statistical distributions of

cloudy updrafts in response to the temperature/moisture perturbations. We will use extensive diagnostics of large-eddy simulations (LESs) with the aid of a tracer-encoding technique. We will then use a stochastic parcel model (SPM) to help interpret the results of the LES. Section 2 provides brief introductions to the models and the tracer-encoding technique, as well as a description of the experiments. As we will show in section 3, the SPM reproduces many of the features of the LES-simulated shallow convection and its responses to temperature and moisture perturbations. We then investigate the evolution history of the parcels in the SPM to identify the physical processes behind the responses (section 3).

In the second half of the paper, we develop the SPM further into a parameterization of shallow cumulus convection, which differs from the previous parameterizations based on bulk entraining/detraining plume models (e.g., Yanai et al. 1973; Kain and Fritsch 1990; Bechtold et al. 2001; Bretherton et al. 2004) or ensemble plume/parcel models (e.g., Arakawa and Schubert 1974; Neggers and Siebesma 2002; Cheinet 2003) but is closer in spirit to episodic mixing models of Raymond and Blyth (1986) and Emanuel (1991). We will introduce the parameterization framework and present simulation results from the parameterization and compare them with the LES results, including the responses to temperature and moisture perturbations (section 4). The main conclusions are then summarized and discussed in the last section.

## 2. Models and experimental design

### a. Models

The LES model used here is Das Atmosphärische Modell (DAM; Romps 2008). It is a three-dimensional, finite-volume, fully compressible, nonhydrostatic, cloud-resolving model. We use a tracer encoding technique to infer the history of cloudy updrafts (Romps and Kuang 2010a,b). Two artificial tracers, called purity and the equivalent potential temperature tracer  $\theta_{e,\text{tracer}}$ , are released at a specified height (tracer release height  $Z_{\text{release}}$ ). At and below  $Z_{\text{release}}$ , the purity tracer is always set to 1 and  $\theta_{e,\text{tracer}}$  of a grid point is always set to its equivalent potential temperature  $\theta_e$ . The two tracers are advected in the same way by the model velocity field, and at every time step both tracers are set to zero for grid points not in the vicinity of cloudy updrafts (cloudy updrafts are defined here as grid points with liquid water content  $q_l$  greater than  $10^{-5}$  kg kg $^{-1}$  and vertical velocity  $w$  greater than 0.5 m s $^{-1}$ ). A grid point is considered to be in the vicinity of cloudy updrafts if it is within a three-grid-point distance from any cloudy updrafts. By reading the value of these tracers at some level above  $Z_{\text{release}}$ , one can infer

some aspects of the updraft's history: the purity tracer estimates the total amount of environmental air entrained, while the ratio of  $\theta_{e,\text{tracer}}$  and purity gives the updraft's  $\theta_e$  value at  $Z_{\text{release}}$ . We shall refer to this ratio as  $\theta_{e,\text{cd}}$ , which stands for encoded equivalent potential temperature. The readers are referred to the above references for some examples of the usages of the tracer encoding technique (e.g., section 2 of Romps and Kuang 2010b).

We shall also use the stochastic parcel model developed in Romps and Kuang (2010a,b) to help understand the results from the LES. This model integrates, forward in time  $\tau$ , the prognostic equations of parcel properties [height  $z(\tau)$ , volume  $V(\tau)$ , temperature  $T(\tau)$ , water vapor content  $q_v(\tau)$ , liquid water content  $q_l(\tau)$ , and vertical velocity  $w(\tau)$ ], given the environmental soundings [temperature  $T_{\text{en}}(z)$  and moisture  $q_{v,\text{en}}(z)$ , where the subscript en denotes an environmental variable] and the initial conditions of the parcels. In this paper, we set the drag coefficient to zero so that updraft velocity is affected only by buoyancy and entrainment. This is done here solely for simplicity, although there have been arguments made for clouds being slippery thermals that experience little drag (Sherwood et al. 2010). The parcel model uses a stochastic entrainment scheme. More specifically, the probability that a moving parcel entrains after a time step  $\Delta\tau$  is

$$P = \Delta\tau|w|/\lambda, \quad (1)$$

where  $\lambda$  is the  $e$ -folding entrainment distance. When entrainment occurs, the ratio of the entrained environmental air mass to the parcel's mass  $f$  has the following probability distribution:

$$\frac{1}{\sigma} e^{-f/\sigma}, \quad (2)$$

where  $\sigma$  is the mean ratio of the entrained mass. Because entrainment is stochastic, a large number of parcels are required to cover the full range of entrainment scenarios in order to obtain statistically significant results.

### b. Experimental design

The shallow cumulus system that we study here is a well-studied oceanic trade cumulus case from the Barbados Oceanographic and Meteorological Experiment (BOMEX). The LES runs have a horizontal and vertical resolution of 25 m, with a horizontal domain size of 12.8 km  $\times$  12.8 km and a vertical extent of 3 km. It is initialized using the initial profiles of temperature, water vapor, and horizontal velocities described in Siebesma and Cuijpers (1995), with some small random noises. The radiative cooling and other large-scale

forcing are also prescribed as in Siebesma and Cuijpers (1995). A bulk parameterization with a drag coefficient of  $1.4 \times 10^{-3}$  is used to calculate the surface fluxes off the 300.4-K ocean surface. Precipitation processes are turned off. The first 3 h of the model run are discarded as spinup. Over the following 2 h, snapshots are saved every 10 min. We then add a temperature or moisture perturbation to each of these snapshots and use them as initial conditions for the perturbed runs. In this way, we produce an ensemble of control and perturbed runs with different initial conditions. We then diagnose the differences between the ensemble averages of the control runs and the perturbed runs.

Three representative perturbations are studied: a 0.25-K temperature anomaly centered at 987.5 m (the T987 case), a 0.5-K temperature anomaly centered at 1262.5 m (the T1262 case), and a 0.2 g kg<sup>-1</sup> moisture anomaly centered at 987.5 m (the Q987 case). The perturbations added are horizontally uniform and Gaussian-shaped in height with a half-width of 75 m. The tails of the Gaussian-shaped anomaly are truncated at levels more than 200 m away from the center. The perturbations are added instantaneously and allowed to evolve freely afterward. Our choice of the size of the perturbations was constrained by the desire to obtain statistically robust results (given the computational constraints) and to limit the extent of nonlinearity. For each case, we have done both runs with positive perturbations and runs with negative perturbations, and the extent of nonlinearity is found to be small. For the T987 case, we have also done runs with a 0.5-K temperature perturbation, which give very similar results to those with a 0.25-K perturbation (times a factor of 2). The only difference is that a peak amplitude of 0.5-K perturbation over 75 m represents a change in stratification that is sufficiently strong to be comparable to the background stratification at this height. This weakens the vertical stratification substantially over the upper half of the perturbation, leading to a local overturning circulation that gives rise to a weak dipole response around 1100 m in the moisture field over the first half hour. To avoid this nonlinearity and for ease of comparison with other cases, we present the results with the 0.25-K perturbation but multiply them by a factor of 2 (Fig. 1). As an example, Fig. 1a shows the positive temperature anomaly for the T987 case. The results shown in next section are the averages of nine members with positive and negative perturbations.

There is one complication with calculating convective responses to perturbations in DAM: as the temperature and moisture perturbations disrupt this balance, the model adjusts to regain hydrostatic balance. The main effect of this adjustment is an instantaneous adiabatic cooling of the layer after the positive temperature and

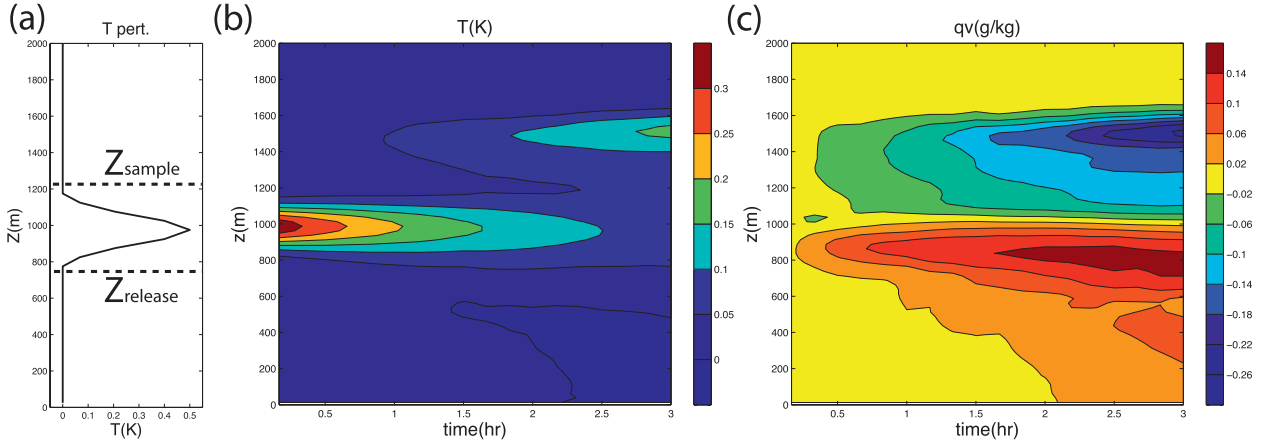


FIG. 1. (a) The initial temperature anomaly of the T987 case. The heights of  $Z_{\text{release}}$  and  $Z_{\text{sample}}$  are also marked. Evolutions of (b) temperature and (c) moisture anomalies after the initial temperature perturbation is introduced. The results are for 0.25-K temperature anomalies and are multiplied by 2 for the plotting.

moisture anomalies are added. For temperature perturbations, this cooling is negligible. However, as we will show in section 3d, convective heating responses to moisture perturbations are remarkably small and the temperature change associated with the hydrostatic adjustment becomes noticeable. We ran DAM in a single column setting to calculate the cooling from this hydrostatic adjustment and corrected for this effect in the results that we present.

We bin the cloudy updrafts based on their purity and  $\theta_{e,\text{ed}}$  to produce two-dimensional (2D) distributions of their properties as functions of those two variables. Taking the T987 case for example, in the LES, the purity and  $\theta_e$  tracers are released at  $Z_{\text{release}} = 762.5$  m (for the T1262 case,  $Z_{\text{release}} = 1037.5$  m, and for the Q987 case,  $Z_{\text{release}} = 762.5$  m). We then sample cloudy updrafts at  $Z_{\text{sample}} = 1212.5$  m (for the T1262 case,  $Z_{\text{sample}} = 1487.5$  m, and for the Q987 case,  $Z_{\text{sample}} = 1212.5$  m) for the 1-h period following the introduction of the anomaly. We then calculate the total mass flux, the mean  $w$ , and  $\theta_e$  of all cloudy updrafts inside each bin defined by the purity and  $\theta_{e,\text{ed}}$  values. These 2D distributions (Figs. 2a–c) provide information on the history of the updrafts traveling through the layer between  $Z_{\text{release}}$  and  $Z_{\text{sample}}$ . The sampling period of the first hour is long enough to give statistically significant results but not too long for the added anomaly to have evolved heavily through convective adjustment. During this period, the properties of the cloudy updrafts at  $Z_{\text{release}}$  are roughly the same for the control runs and the perturbed runs. Therefore, differences in the distributions at  $Z_{\text{sample}}$  (Figs. 3a–c) give responses of cloudy updrafts to the introduced temperature anomaly.

We compute the same diagnostics for the SPM. The parcels in the SPM are viewed as analogs of the cloudy

updraft grid points in the LES. Millions ( $\sim 1$  million in this study) of parcels are released at  $Z_{\text{release}}$  in the SPM. Two conditions need to be specified for the SPM: the initial conditions at  $Z_{\text{release}}$  and environmental profiles between  $Z_{\text{release}}$  and  $Z_{\text{sample}}$ . To assign them appropriate initial conditions, we sample 100 LES snapshots to get a 3D PDF of the cloudy updrafts at  $Z_{\text{release}}$  as functions of  $w$ ,  $T$ , and  $q_r$ . The PDFs at  $Z_{\text{release}}$  from the LES are found to be similar between the control and the perturbed runs. In the SPM, we shall use the PDFs from the LES control runs for both the control and the perturbation runs. The initial conditions of the parcels are drawn randomly from this 3D PDF. This procedure ensures that the parcels in the SPM have the same statistical properties as updrafts in the LES at  $Z_{\text{release}}$ . For the control run of the SPM, the environmental sounding is the ensemble mean sounding of the LES control runs. For the perturbed runs of the SPM, we add the same perturbations as in the LES perturbation runs. We also follow the same sampling processes at  $Z_{\text{sample}}$ . In the SPM, the purity of a parcel is the ratio of its mass at  $Z_{\text{release}}$  to its mass at  $Z_{\text{sample}}$ , and parcels' initial  $\theta_e$  at  $Z_{\text{release}}$  takes the place of  $\theta_{e,\text{ed}}$  in the LES. In the figure axes, we call it “initial  $\theta_e$ ” to remind readers that it is an SPM-generated result.

Because the pair of parameters  $[\lambda, \sigma]$  mainly controls the entrainment process, we briefly discuss how they are chosen. Romps and Kuang (2010b) surveyed a large range of combinations of  $\lambda$  and  $\sigma$ . They defined an objective function based on mass flux agreement between the LES and the SPM and searched the best fitting  $\lambda$  and  $\sigma$ , namely  $\lambda = 226$  m and  $\sigma = 0.91$ , that minimize the objective function. They also note that there is a valley in the  $[\lambda, \sigma]$  space, where pairs of  $[\lambda, \sigma]$  give very similar values of the objective function. For pairs of parameters

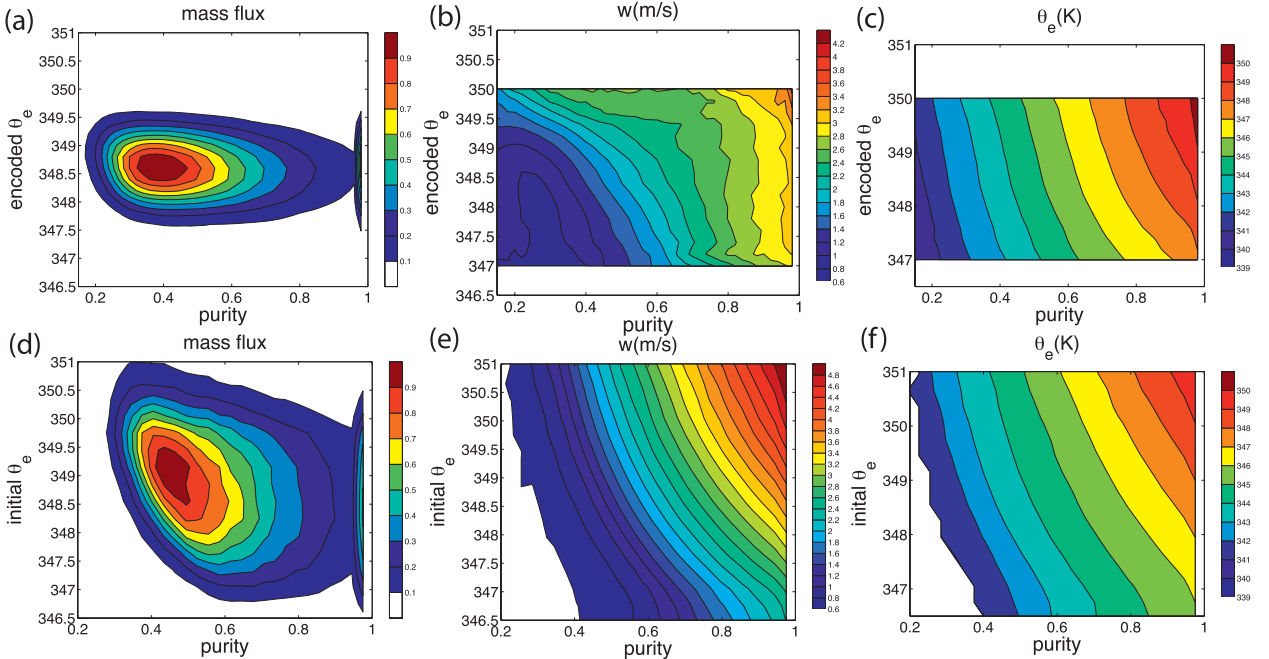


FIG. 2. Cloudy updraft statistics of the LES control run: (a) mass flux, (b)  $w$ , and (c)  $\theta_{e,ed}$  shown as functions of purity and  $\theta_{e,ed}$ . The mass flux distributions are normalized to range from 0 to 1. (d)–(f) As in (a)–(c), but from the SPM control run.

that are along this valley, although the total amount of mass flux is similar, the distribution of mass flux in terms of purity is quite different. For example, the parameters used in Romps and Kuang (2010b) allow too many undiluted updrafts compared to the distributions from our current 25-m resolution run (Fig. 2a), even though their parameters are consistent with the total amount of mass flux and purity. We have chosen  $\lambda = 125$  m and  $\sigma = 0.32$  to give a mass flux distribution as a function of purity (Fig. 2d) that matches the distribution from the current LES simulations (Fig. 2a).

### 3. Response to temperature and moisture perturbations

#### a. Responses in the T987 case

For a temperature perturbation centered at 987.5 m, the amplitude of the initially added temperature anomaly decreases by a factor of 2 in about 30 min (Fig. 1b), an example of the convective adjustment process. In addition, there is slight warming in the trade inversion around 1600 m. Moisture responses (Fig. 1c) show that layers below 987.5 m experience moistening and layers above experience drying. The moistening propagates downward toward the surface with time. The basic features of the responses can be understood in terms of inhibition of cloudy updrafts by the added temperature anomaly, which cools this region and reduces the initial

temperature perturbation. The reduced penetrative entrainment in the inversion layer also leads to the warming near 1600 m. Furthermore, the enhanced detrainment in and below the region of the temperature perturbation leads to the moistening, while the reduced detrainment above leads to the drying.

We now investigate changes in the statistics of cloudy updrafts. The mass flux distribution of the LES control run (Fig. 2a) is mostly located between 347.5 and 349.5 K on the  $\theta_{e,ed}$  axis, reflecting variations of updrafts' properties at  $Z_{release}$ . The mass flux is mostly located between 0.2 and 1.0 on the purity axis, while the maximum lies around 0.45. This indicates that most updrafts mix with environmental air when they go across the layer between  $Z_{release}$  and  $Z_{sample}$ . However, there are some undiluted updrafts with purity close to 1 (here “undiluted” is relative to  $Z_{release}$ , not to the cloud base). The SPM-generated mass flux distributions (Fig. 2d) show general similarities. We find that the LES mass flux distribution has a narrower range in  $\theta_{e,ed}$  than that of the SPM. The narrowing is due to in-cloud mixing in the LES, which homogenizes the initial identities of the air that makes up the updrafts. In our SPM, in-cloud mixing is not included at the moment for simplicity. In-cloud mixing is a process that we would like to add into the SPM in the future, perhaps following the approach of Krueger et al. (1997).

The distributions of the LES simulated  $w$  and  $\theta_e$  are plotted in Figs. 2b and 2c. Both  $\theta_e$  and  $w$  show a tilted



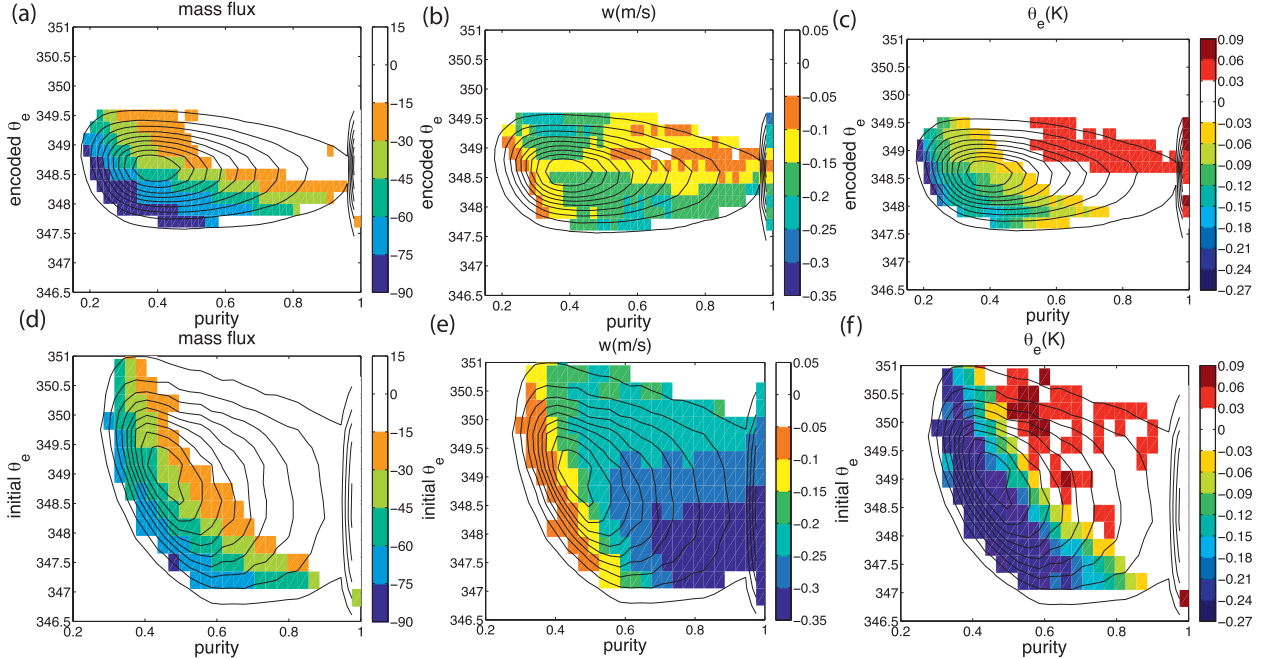


FIG. 3. Color indicates (a) LES-simulated fractional changes in mass flux (%), and changes in (b)  $w$  and (c)  $\theta_e$  in the T987 case as functions of purity and  $\theta_{e,cd}$ . The background black contours are the LES control run mass flux plotted in Fig. 2a. (d)–(f) As in (a)–(c), but for the SPM. The background black contours are the SPM control run mass flux plotted in Fig. 2d. Color values outside the lowest black contour are zeroed out.

structure with their values increasing from the lower left to the upper right of the figures. This is simply because parcels that initially have higher  $\theta_{e,cd}$  or entrain less environmental air (and thus have higher purity) will end up with higher  $\theta_e$  and also achieve higher  $w$  values due to stronger buoyancy acceleration and less slow-down by entrainment. We have also plotted the same distributions for total water content  $q_t$  and buoyancy  $b$ . They show similar tilted patterns as  $\theta_e$  (figures are not shown).

The SPM-generated  $w$  and  $\theta_e$  distributions (Figs. 2e,f) show a similar gradient. Closer inspection shows that the agreement in  $w$  is not as good as that in  $\theta_e$ . More specifically, the constant  $w$  contours of the LES distribution are almost vertical in regions of high purity (Fig. 2b), indicating little dependence of  $w$  on the encoded  $\theta_e$ . For high encoded- $\theta_e$  values, the dependence of  $w$  on purity is also somewhat weakened (constant  $w$  contours being more horizontal).

We speculate that the discrepancy between the LES and the SPM is because of the intracloud interaction between updrafts. In our LES simulations, the resolution is relatively high and clouds are well resolved. The cloudy parcels can exchange momentum through pressure gradient force in addition to actual mixing of fluids. This could cause momentum exchange between the most active cloud cores (which tend to be binned into

the upper-right corner in Fig. 2b) and the cloudy parcels surrounding them (which tend to be binned into the upper-left and lower-right parts in Fig. 2b), while keeping their thermodynamic properties such as  $\theta_e$  unchanged. We have tried coarsening the 3D outputs to a lower resolution before generating the statistics shown in Figs. 2a–c (the R25-b runs listed in Table 1). We have also made runs with the same settings as the control but at lower resolutions (the R100 runs listed in Table 1). The results are described in the appendix, where we show that in both cases (rows 1 and 4 in Fig. A1) the  $w$  distribution is more similar to the SPM results and to that of  $\theta_e$ . On the other hand, runs with higher resolutions (also described in the appendix and shown in row 3 in Fig. A1) give results similar to our control. We speculate that in the lower-resolution runs, clouds are less well resolved so that the disparity in the intracloud homogenization of momentum and thermodynamic properties is reduced.

To test this idea, we calculate the correlation between  $w$  and  $\theta_e$  for the cloudy updrafts. Using 60 snapshots from the control runs and also 60 snapshots from the low-resolution runs (R100 runs as in Table 1), we found that the overall correlation between  $w$  and  $\theta_e$  of the cloudy updrafts is 0.57 for the control runs, while for the low-resolution runs it is 0.75. This is in line with the results that  $w$  and  $\theta_e$  have more similar patterns in the low-resolution runs than in the high-resolution runs. We have

TABLE 1. Summary of the numerical experiments used in the sensitivity tests.

| Simulation | Resolution (m; $\Delta x \times \Delta y \times \Delta z$ ) | Tracer-protecting halo size (m) | Remarks                           |
|------------|---|---------------------------------|-----------------------------------|
| R100       | $100 \times 100 \times 50$                                  | 300                             | Control run of the paper          |
| R25-a(CTL) | $25 \times 25 \times 25$                                    | 75                              |                                   |
| R12.5      | $12.5 \times 12.5 \times 12.5$                              | 75                              |                                   |
| R25-b      | $25 \times 25 \times 25$                                    | 75                              | Coarsened resolution for sampling |
| R25-c      | $25 \times 25 \times 25$                                    | 300                             |                                   |

further separated the  $w$  and  $\theta_e$  variations into intracloud and intercloud components. The correlation for intercloud variations of  $w$  and  $\theta_e$  are 0.62 for both the control and the low-resolution runs, while the correlation for intracloud variations is 0.54 for the control runs, significantly smaller than that of the low-resolution runs (0.78). While these results are in line with our argument, more detailed studies are clearly needed to fully understand the differences seen between the high- and low-resolution runs. Note also that in the low-resolution runs, the peak mass flux has a higher purity than that of the control runs (0.6 vs 0.45), indicating reduced entrainment because of the lower resolution.

Changes in the above statistics in the perturbed runs as compared to the control run are plotted in Fig. 3. Figure 3a shows the fractional change in cloudy updraft mass flux in response to the perturbation. It is clear that updrafts with low initial  $\theta_e$  and those that entrain heavily (thus having low purity) are preferentially removed by the temperature perturbation. The mass flux of updrafts with high initial  $\theta_e$  and those less diluted by entrainment are less affected. The contours of constant fractional change in mass flux are almost along the contours of  $\theta_e$  (Fig. 2c), indicating the controlling influence of buoyancy (for saturated air,  $\theta_e$  is a good proxy for buoyancy): the temperature anomaly forms a buoyancy barrier that preferentially inhibits updrafts with low buoyancy.

Responses in  $w$  (Fig. 3b) are negative over most regions, mainly because the temperature perturbation decreases the height-integrated buoyancy (or potential energy) available to the updrafts. The SPM-generated  $w$  responses are also all negative. The smaller decrease in  $w$  for updrafts with lower purity is because parcels that entrain heavily gain additional buoyancy from the environmental temperature anomaly. The reference state  $w$  shown in Figs. 2b and 2e also affects the  $w$  responses. As changes in the height-integrated buoyancy or potential energy available to the updrafts are linearly related to changes in  $w^2$ , a higher reference state  $w$  implies a smaller change in  $w$  for the same change in the height-integrated buoyancy. In regions with strong fractional decrease in mass flux (i.e., the lower-left corner), changes in the height of entrainment events also contribute to the smaller  $w$  decrease, as will be discussed in section 3b. The less-negative

patch in the upper-right part of the LES-simulated  $w$  responses is not captured by the SPM and is not understood. We speculate that the buoyancy barrier associated with the positive temperature perturbation may inhibit intracloud momentum transport and lead to this less-negative patch. More studies into this behavior are clearly needed. Intriguingly, this less-negative patch is not seen in the lower-resolution LES simulations (not shown).

Cloudy updrafts with high  $\theta_{e,ed}$  or high purity (the upper-right part of the PDF), in which there is little mass flux change, show a slight increase in their  $\theta_e$  due to entrainment of warmer environmental air (Fig. 3c). On the other hand, updrafts with lower  $\theta_{e,ed}$  and lower purity (the lower-left part of the PDF), in which there is a significant fractional decrease in mass flux, show a decrease in their  $\theta_e$  (Figs. 3c,f). The reason for this will be discussed in section 3b.

The responses of SPM-generated statistics (Figs. 3d–f) are generally similar to those of the LES. Given the simplicity of the SPM and the complexity of the cloud field, we do not expect the SPM to reproduce every feature of the LES statistics (the tracer-encoding technique also has its own deficiencies.) However, the SPM does capture the main responses of statistics, such as the decreases of mass flux in the lower-left region, the general decreases of  $w$ , the decreases of  $\theta_e$  in the lower-left, and the increases of  $\theta_e$  in the upper-right region.

For a fair comparison with the LES, the evolving soundings during the first hour of the LES perturbation runs were used in the SPM for the results shown in Figs. 3d–f. We have also performed SPM experiments where the environmental soundings are kept constant in time (LES control sounding plus the initial perturbation). The results are very similar to those shown in Figs. 3d–f, except with larger amplitudes (not shown). This is simply because the temperature anomaly in the LES decays significantly over the 1-h sampling period, instead of maintaining its initial amplitude (Fig. 1b).

The stochasticity of the entrainment process is key for the SPM to match the LES results. To highlight this point, we designed another experiment in which we run the SPM with constant entrainment of  $\epsilon = 1.8 \times 10^{-3} \text{ m}^{-1}$  instead of the stochastic entrainment. We choose this

constant entrainment rate to give a similar amount of overall entrainment as in the stochastic entrainment case. For ease of interpretation, in this pair of experiments we fix the environmental sounding to be the initial perturbed sounding to eliminate effects from changes in the environmental sounding. Other settings such as initial conditions of the parcels are unchanged. Because for the constant entrainment case the purity of parcels sampled at  $Z_{\text{sample}}$  is the same, we only plot mass flux distribution as a function of  $\theta_{e,\text{cd}}$ . The PDFs of the SPM with constant entrainment, the SPM with stochastic entrainment, and the LES are shown in Fig. 4 (summing Figs. 2a and 2d along the purity axis gives the black lines in Figs. 4c and 4b, respectively). With the constant entrainment, the fate of a parcel is determined by its initial conditions. With the temperature perturbation, there is a threshold of around 348.5 K in terms of the initial  $\theta_e$ . Mass fluxes of updrafts with initial  $\theta_e$  below the threshold are totally cut off, while mass fluxes with initial  $\theta_e$  above the threshold are not affected at all. The threshold has a finite width because the initial conditions of the updrafts have variations in  $w$ , which are not reflected on the initial  $\theta_e$  axis. On the other hand, the decrease of LES mass flux is over almost all ranges of  $\theta_{e,\text{cd}}$ , although the mass flux with lower  $\theta_{e,\text{cd}}$  decreases more. The LES results are much more similar to the SPM results with stochastic entrainment (Fig. 4b). This analysis indicates that stochastic entrainment is essential in the parcel model and more realistic than constant entrainment.

### b. The height of entrainment

We now analyze the parcels' evolution history in the SPM to understand the decreases of  $\theta_e$  and their collocation with decreases of mass flux in the lower-left half of Figs. 3c,f. It turns out that decreases of mass flux and composite  $\theta_e$  are due to one single mechanism.

We plot the trajectories of randomly selected parcels reaching  $Z_{\text{sample}}$  with a purity of 0.6 in the phase space of  $Z$  and purity (Fig. 5). In other words, we are looking at one thin band of the distribution around a purity of 0.6 in Fig. 3d. The purities of parcels at  $Z_{\text{release}} = 762.5$  m are 1.0 by design. A sudden decline of purity indicates an entrainment event. In the control runs, entrainment events are roughly uniformly distributed in height. However, in the perturbed runs, most parcels reaching  $Z_{\text{sample}}$  experience entrainment at relatively high altitudes. Since the entrainment probability functions are the same, we infer that in the perturbed case the parcels that entrain heavily at lower heights cannot penetrate the perturbation layer to be sampled.

The above analysis indicates that the height at which an air parcel entrains is important in determining its fate. To further illustrate this point, we perform the following

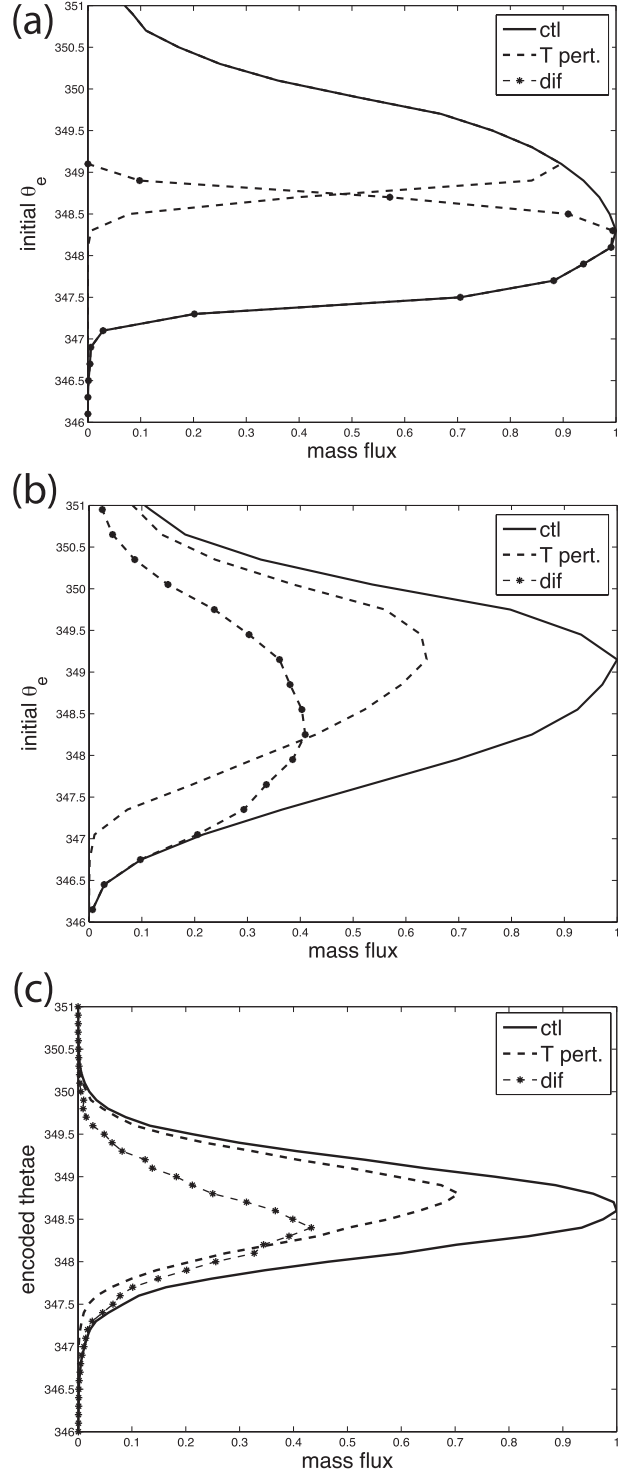


FIG. 4. The SPM-generated distribution of mass flux as a function of  $\theta_{e,\text{cd}}$  with (a) constant entrainment and (b) stochastic entrainment. (c) LES-generated distributions. The solid and dashed lines represent the control and the perturbed runs, respectively, and the differences are shown in the lines with asterisks.



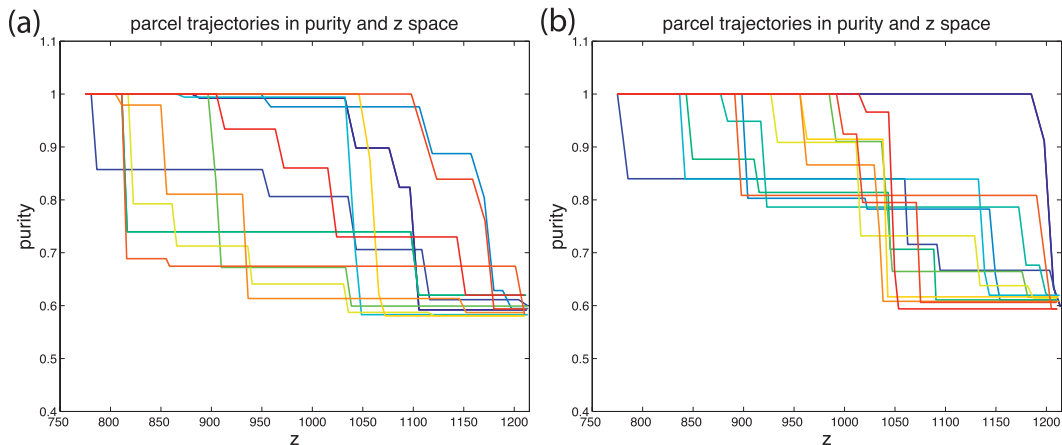


FIG. 5. The trajectories of parcels with purity between 0.58 and 0.62 at  $Z_{\text{sample}}$ , for the (a) controlled and (b) perturbed runs. Each line represents one trajectory. For each run, only 12 trajectories, which are randomly chosen, are plotted for readability.

experiment. We release a parcel at  $Z_{\text{release}} = 762.5$  m with initial conditions of  $T = 293.67$  K,  $q_i = 16.82$  g kg $^{-1}$ , and  $w = 1.32$  m s $^{-1}$ , which are the mean properties of the cloudy updrafts at  $Z_{\text{release}}$  in the LES. While traveling toward  $Z_{\text{sample}}$ , this parcel entrains only once. The single entraining event will dilute the parcel to a purity of 0.6. We release the same parcel a number of times and each time have the parcel entrain at a different height between  $Z_{\text{release}}$  and  $Z_{\text{sample}}$ , separated by an interval of 30 m. This experiment eliminates variations in the initial conditions. It also simplifies the stochastic entrainment treatment by emphasizing only one aspect: for a parcel that entrains the same amount of environmental air, it may entrain at different heights. In the perturbed run, we again set the environmental sounding to be the initial perturbed sounding and keep it constant in time.

We plot the trajectories of these parcels in the phase space of  $Z$  and  $w$  (Fig. 6). The uppermost line is the trajectory of an undiluted parcel. A sudden decline in  $w$  indicates an entrainment event because the parcel entrains environmental air with zero  $w$ . For the control run, if the parcel entrains below about 850 m, it becomes negatively buoyant and also descends. If it entrains above 850 m, it is temporarily negatively buoyant after entrainment. However, after continued ascent by inertia for a certain distance, it becomes positively buoyant and accelerates upward.

With the temperature perturbation, the critical height that separates rising and descending trajectories is higher than that of the control run, reaching about 1035 m (Fig. 6b). Thus, in the perturbed run, parcels that entrain at lower altitudes are filtered out. The remaining parcels preferentially entrain at higher altitudes where the environmental  $\theta_e$  is lower. As a result, the updrafts'  $\theta_e$  sampled at

$Z_{\text{sample}}$  decreases. This is why in Fig. 4c the composite  $\theta_e$  decreases in regions with significant decreases in mass flux. This preference for parcels that entrain at higher altitudes also contributes to the smaller  $w$  decrease in the lower-left part of Figs. 3b,e. This is because these parcels enjoy undiluted buoyancy acceleration over a longer distance and thus attain higher kinetic energy. While parcels that entrain at higher altitudes also lose more kinetic energy because they have greater  $w$  at the time of entrainment, this effect is weaker compared to the buoyancy effect. Thus, the preferential elimination processes described above have the effect of increasing the composite updrafts'  $w$ . This effect is most significant where there is substantial fractional mass flux decrease. Our analysis shows that in the region with fractional mass flux decreases over 60%, this elimination process has an effect on  $w$  that is nearly equal to the effect of additional buoyancy gained by entraining warmer environmental air.

The above analysis is only for parcels with one set of initial conditions and purity. One can do similar calculations for parcels with different initial conditions and purities. If the temperature perturbation can effectively lift the critical height, then it will decrease the mass flux and  $\theta_e$  of the composite updrafts reaching  $Z_{\text{sample}}$ . It will also partially compensate for the slowdown of the composite updrafts reaching  $Z_{\text{sample}}$  due to the decrease in the height-integrated buoyancy.

### c. Responses in the T1262 case

We have performed the same analyses as in the previous subsection for the T1262 case. While for the T987 case, we ran the simulation for 3 h to provide a sense of longer time evolution of the anomalies, because of limited computational resources we ran the T1262 case and the

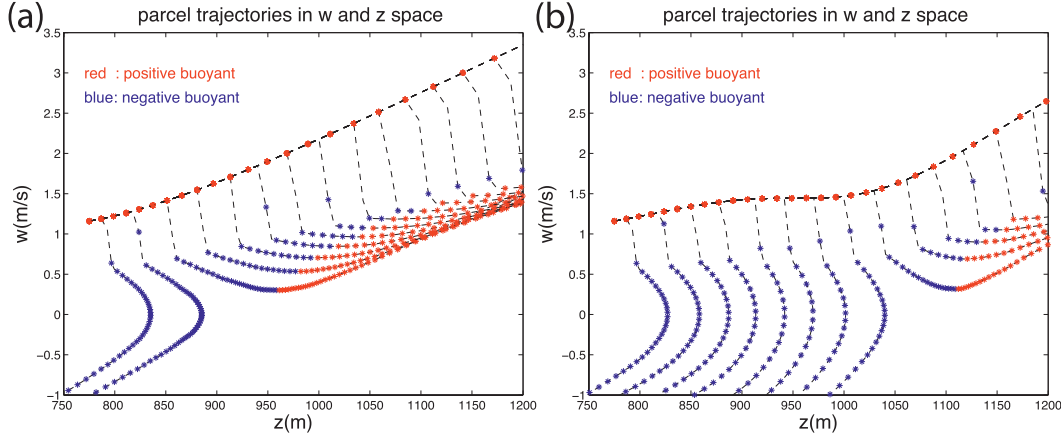


FIG. 6. The trajectories of parcels that entrain the same amount of environmental air but at different heights, for the (a) controlled and (b) perturbed runs. The blue dots indicate negative buoyancy; red dots indicate positive buoyancy.

Q987 case described in the next subsection only for 1 h, which is the period over which we sample the statistics of the cloudy updrafts.

The evolution of the large-scale environment is shown in Fig. 7. Its responses are generally similar to the T987 case: strong local cooling and moistening below and drying above the perturbation. The responses of the distributions of cloudy updraft properties and the comparison between the LES and the SPM (Fig. 8) also share many similarities with the T987 case, which indicates that the mechanisms discussed in the T987 case also operate in the T1262 case.

The main difference between these two cases is that the decay of the initially imposed anomaly is slower in the T1262 case than in the T987 case. Because the fractional changes in mass flux are similar in the T987 and

T1262 cases, it is presumed here that the different decay rates are because the background (control run) liquid potential temperature  $\theta_l$  flux convergence at 1262.5 m is smaller than at 987.5 m so that changes in the  $\theta_l$  flux convergence caused by the temperature perturbation at 1262.5 m are also smaller than at 987.5 m. On the other hand, the background  $q_l$  flux convergence at 1262.5 m is of a similar magnitude as that at 987.5 m, so the moisture responses in the T1262 case (Fig. 7b) is comparable to that in the T987 case (Fig. 1c).

#### d. Responses in the Q987 case

The responses to moisture perturbations are quite different from those to temperature perturbations. The added moisture anomaly is also damped as expected

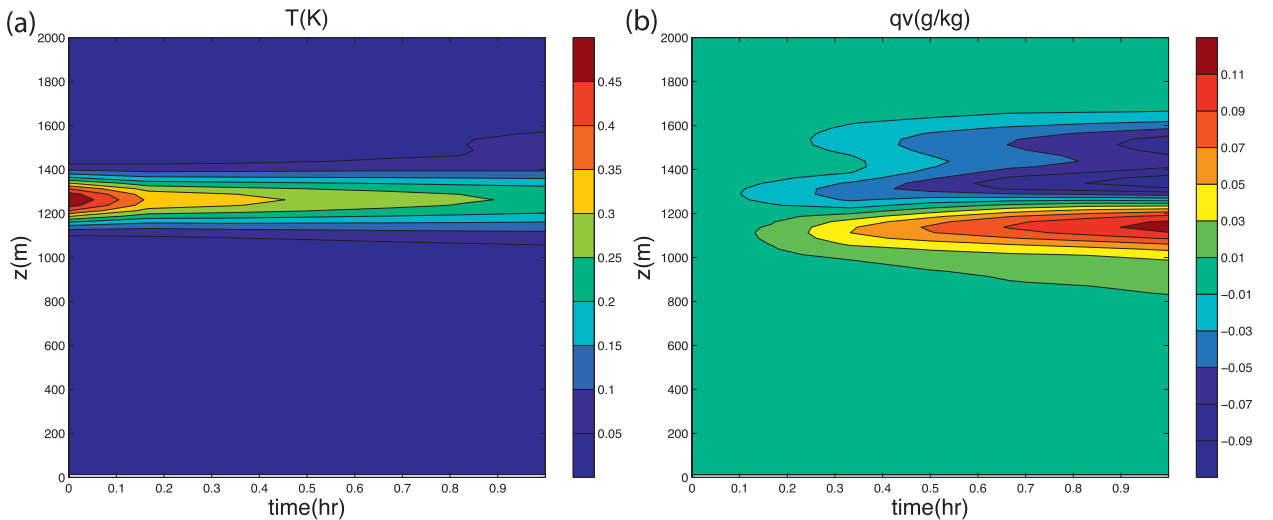


FIG. 7. As in Figs. 1b and c, but for the T1262 case. Note that it only shows evolution of the soundings over the first hour after the perturbation is added.

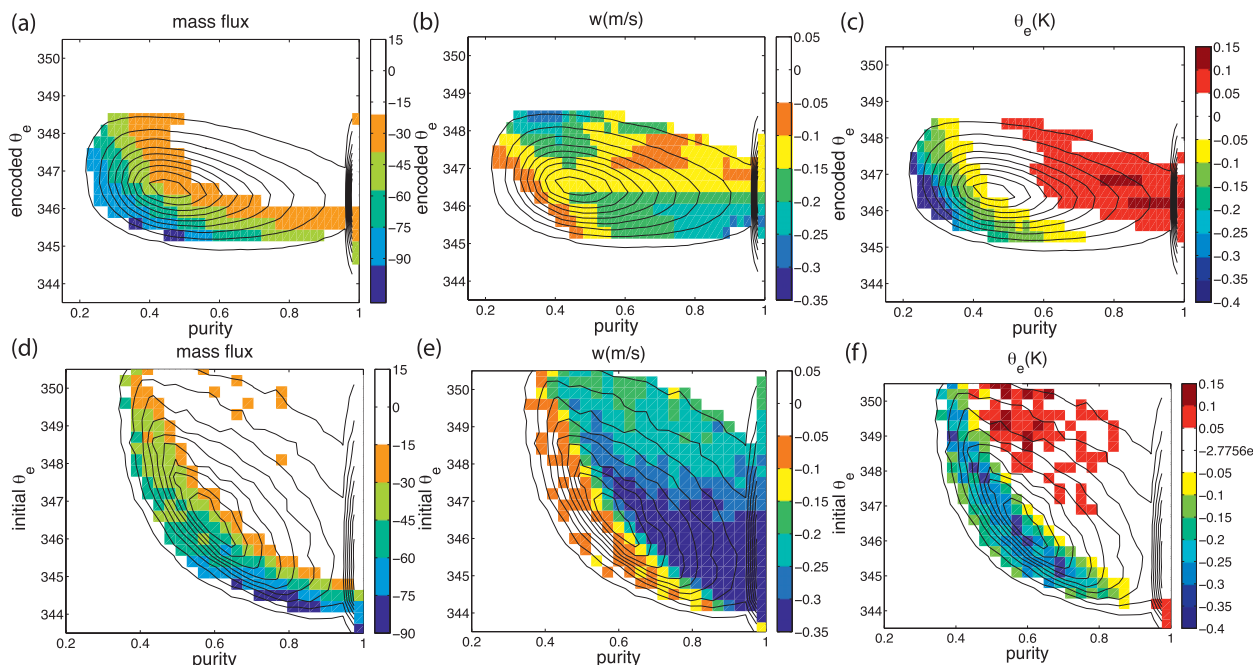


FIG. 8. As in Fig. 3, but for the T1262 case.

(Fig. 9b). However, the temperature responses are remarkably small, on the order of  $10^{-3}$  K. Note that we have corrected for the effect of the hydrostatic adjustment (which produces a negative temperature anomaly with a peak amplitude of  $9.5 \times 10^{-3}$  K and the same shape as the added moisture anomaly) as discussed in section 2b. The temperature in the perturbed layer increases with time, while there is cooling centered around

1500 m in the inversion layer. These changes are consistent with an enhancement of cloudy updrafts by the added moisture anomaly, which warms the perturbed layer and causes the cooling near 1500 m through penetrative entrainment in the inversion layer.

Statistics of cloudy updrafts again show general agreement between the LES and the SPM (Fig. 10). Both LES and SPM show that mass flux in the low purity and low

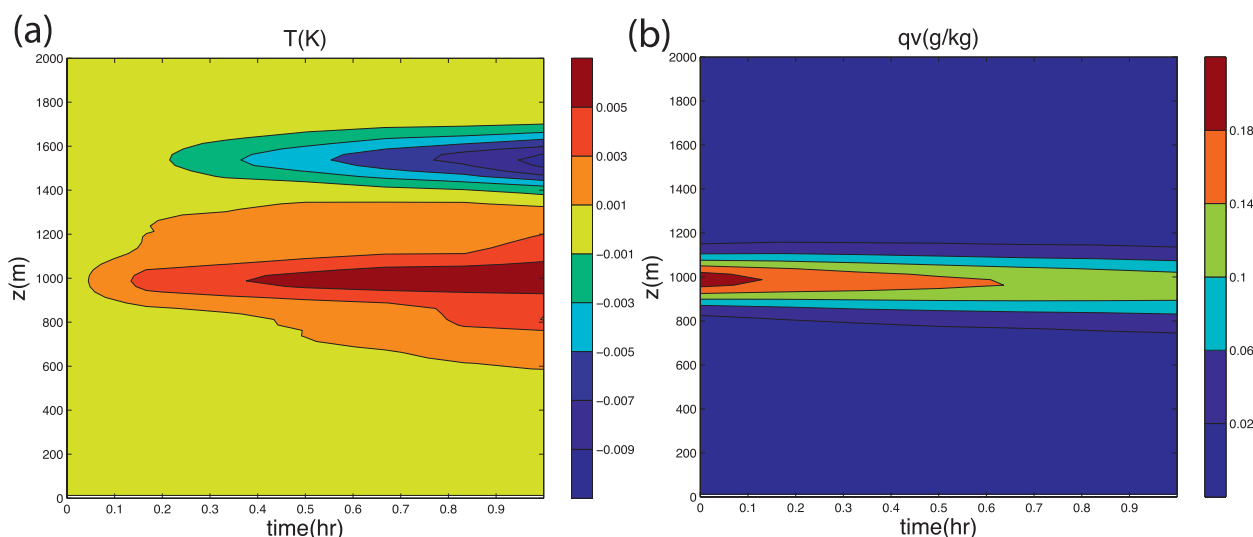


FIG. 9. As in Figs. 1b and c, but for the Q987 case. Note that it only shows evolution of the soundings over the first hour after the perturbation is added.

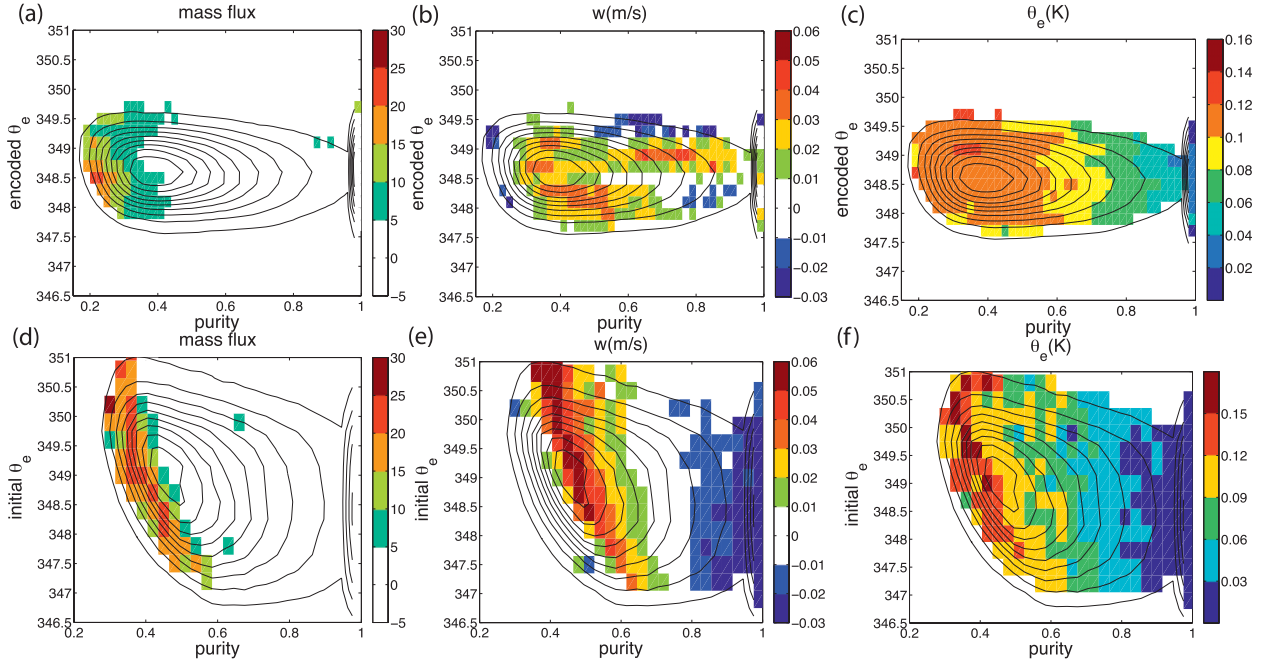


FIG. 10. As in Fig. 3, but for the Q987 case.

$\theta_{e,ed}$  region increases while mass flux in the other regions is mostly unchanged. It indicates that a moister environment benefits less buoyant updrafts by increasing their  $\theta_e$ . The  $w$  distribution of the SPM shows an increase over a tilted band with purity around 0.5. Over the area with purity close to 1.0,  $w$  is decreased because the moisture perturbation increases environmental buoyancy slightly, which decreased height-integrated buoyancy (or potential energy) available to undiluted parcels. The  $w$  signal of the LES is relatively noisy. It also shows increases in the region with medium purity values, similar to that of the SPM. There is also a hint of  $w$  increase near purity of 0.8, which is not captured by the SPM. The  $w$  increase in the region with medium purity values is because of the entrainment of higher  $\theta_e$  air, which boosts the parcel/updraft buoyancy and increases its vertical velocity. This effect is significant only for parcels/updrafts that experience significant entrainment. For parcels that entrain too heavily (i.e., those with the lowest purity values), however, the same effect of entrainment height selection discussed in section 3b comes into play: with a positive moisture perturbation to the environment, parcels/updrafts that entrain at lower altitudes and could not reach the sampling height can now reach it. These parcels have had undiluted buoyancy acceleration over shorter distances and thus lower vertical velocities, weighting down the average  $w$  of parcels with low purities. For both LES and SPM,  $\theta_e$  shows general increases over all the regions because the moisture anomaly increases environmental  $\theta_e$ . For

updrafts with lower purity, the increase in  $\theta_e$  is larger because these are parcels that entrain more.

The reason that responses in mass flux and heating are very small for the moisture perturbation is that moisture anomalies are inefficient in changing the buoyancy of either the environmental air or the updrafts. Note that a  $0.2 \text{ g kg}^{-1}$  specific humidity change is similar to a 0.5-K temperature in terms of the change to the equivalent potential temperature. To illustrate this point, we plot the mixing diagrams (as in, e.g., Bretherton et al. 2004) of a typical parcel with environmental soundings of the control, T987, and Q987 cases at the 987.5-m height (Fig. 11). The parcel has  $T = 293.67 \text{ K}$ ,  $q_t = 16.82 \text{ g kg}^{-1}$  at  $Z_{\text{release}} = 762.5 \text{ m}$  and is taken to rise undiluted to 987.5 m and then mix with the environment. With the temperature anomaly, the environmental density decreases significantly so that almost all mixtures are negatively buoyant. However, differences between the mixing lines of the control and Q987 cases are very small. The environmental density is decreased slightly with the moisture anomaly, shown as the slight descent of nonmixed points with  $\chi = 0$  ( $\chi$  is the fraction of environmental air in the mixture). The  $\chi$  value corresponding to neutral buoyancy only shifts rightward slightly with the moisture anomaly. When normalized by their contributions to moist static energy anomalies, moisture anomalies are not efficient in changing updrafts' fate in the BOMEX case, compared to temperature anomalies.

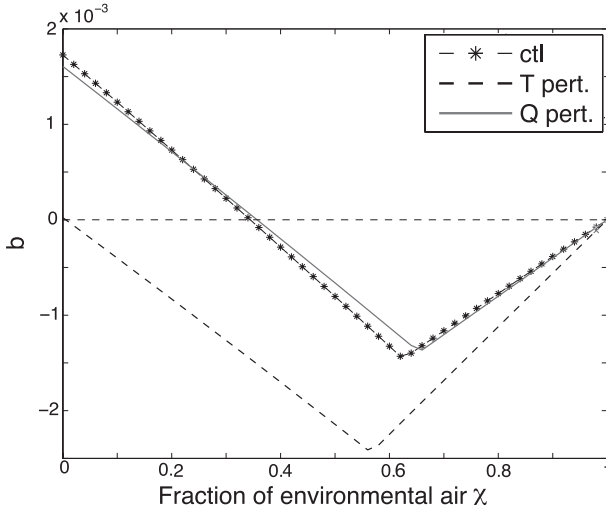


FIG. 11. Buoyancies, divided by gravitational acceleration, (i.e., minus the fractional density anomaly  $b$ ) of a typical cloudy updraft parcel after mixing different fractions  $\chi$  of environmental air at 987.5 m. A value of  $b > 0$  indicates positive buoyancy. The dot-dashed line uses the environmental sounding from the control runs, the dashed line uses the T987 sounding, and the solid line uses the Q987 sounding.

#### 4. A shallow convective parameterization based on stochastically entraining parcels

##### a. Constructing the parameterization scheme

The basic function of a convective parameterization is to use large-scale variables to estimate tendencies of mass, heat, moisture, momentum, and other tracers due to convective motions. A moist convective parameterization typically contains the following two key components. The first is the determination of cloud-base conditions, and the second is a cloud model that describes the evolution of clouds as they rise above the cloud base, a key being their interactions with the environmental air.

A variety of approaches have been used for the cloud model, including, for example, a bulk constant entrainment plume or an ensemble of plumes with fixed entrainment rates (e.g., Simpson 1971; Arakawa and Schubert 1974; Tiedtke 1989; Bechtold et al. 2001). Some parameterizations include some coupling between entrainment and updrafts, an example being the buoyancy sorting approach (Raymond and Blyth 1986; Kain and Fritsch 1990; Bretherton et al. 2004). The stochastic entrainment method used in this study provides another approach to represent the mixing processes. This method explicitly simulates the stochastic nature of mixing, specified through the two probability functions [Eqs. (1) and (2)] described earlier in section 2.

The determination of the cloud-base conditions is what we need to extend the SPM into a parameterization. We shall follow a treatment similar to Cheinet (2003) and

represent convective transport in the subcloud layer and that in the cloud layer within a single framework. By doing so, we are assuming that fluxes in the subcloud layer are dominated by surface-generated eddies and the subcloud layer turbulent fluxes can also be parameterized by the stochastic parcel model.

We shall release parcels directly from the near-surface layer (the lowest model level  $Z_s$ ). The statistical distributions of these parcels' initial conditions ( $m$ ,  $T$ ,  $q_v$ , and  $w$  at  $Z_s$ ), where  $m$  is the mass of the parcel, will be determined by the surface fluxes [sensible heat flux  $F_H$  and latent heat flux  $F_L$  ( $\text{W m}^{-2}$ )] and surface layer statistics. The treatment follows closely that of Cheinet (2003) and is described below for completeness.

Variations in  $T$ ,  $q_v$ , and  $w$  near the surface are approximated by Gaussian distributions. In addition, both measurements and LES diagnostics show that near the surface  $w$ ,  $T$ , and  $q_v$  are strongly correlated with each other. Let  $C_{XY}$  be the correlation coefficient between  $X$  and  $Y$ . We shall treat  $C_{wT}$ ,  $C_{wq}$ , and  $C_{Tq}$  as given parameters.

First, we assume that  $w$  follows a Gaussian distribution  $s$  with a zero mean and a standard deviation of  $\sigma_w$ :

$$s = \frac{1}{\sqrt{2\pi}\sigma_w} \exp\left(-\frac{w^2}{2\sigma_w^2}\right), \quad (3)$$

where  $\sigma_w$  is specified using Eqs. (A3) and (A4) in the appendix of Cheinet (2003):

$$\sigma_w = 1.9 \left( \kappa g Z_s \frac{F_H}{\bar{T} c_{pa}} \right)^{1/3}, \quad (4)$$

and  $\kappa = 0.4$  is the von Kármán constant,  $c_{pa}$  is the dry air heat capacity at constant pressure,  $\bar{T}$  is the mean environmental temperature at  $Z_s$ , and  $g$  is the gravitational acceleration.

We now describe how to infer distributions of  $T$  from the surface sensible heat flux. We shall describe  $T$  as

$$T = \bar{T} + \frac{\sigma_T}{\sigma_w} C_{wT} w + x, \quad (5)$$

where  $\sigma_T$  is the standard deviation of temperature and  $x$  represents a white noise and is independent of  $w$  with a standard deviation of  $\sigma_x$ . From the definition of  $\sigma_T$  and  $C_{wT}$ , we have

$$\sigma_T^2 = C_{wT}^2 \sigma_w^2 + \sigma_x^2, \quad (6)$$

$$\sigma_w \sigma_T C_{wT} = \int w(T - \bar{T}) s dw = \frac{F_H}{\bar{\rho} c_{pa}}. \quad (7)$$



In the above equation, the density of each parcel is approximated by the environmental mean density  $\bar{\rho}$  in calculating  $F_H$ . The same approximation is applied later in Eq. (10). Given surface  $F_H$ ,  $\sigma_T$  and  $\sigma_x$  can be calculated from Eqs. (6) and (7).

The procedure to infer distributions of  $q_v$  is similar to that of  $T$ . We shall describe  $q_v$  as

$$q_v = \bar{q}_v + \frac{\sigma_q}{\sigma_w} C_{wq} w + \frac{\sigma_q}{\sigma_x} C_{xq} x + y, \quad (8)$$

where  $\bar{q}_v$  is the mean environmental specific humidity,  $\sigma_q$  is the standard deviation of  $q_v$ , and  $y$  is a white noise independent of both  $w$  and  $x$ . In addition, from the definition of  $\sigma_q$  and  $C_{wq}$ , we have

$$\sigma_q^2 = C_{wq}^2 \sigma_q^2 + C_{xq}^2 \sigma_q^2 + \sigma_y^2, \quad (9)$$

$$\sigma_w \sigma_q C_{wq} = \int w(q_v - \bar{q}_v) s dw = \frac{F_L}{\bar{\rho} L}, \quad (10)$$

where  $L$  is the latent heat of vaporization. From Eqs. (5) and (8), we have

$$C_{qT} = C_{wT} C_{wq} + \frac{C_{xq} \sigma_x}{\sigma_T}. \quad (11)$$

At this point  $\sigma_q$ ,  $\sigma_y$ , and  $C_{xq}$  can be solved from Eqs. (9)–(11). As a summary, given inputs  $F_H$ ,  $F_L$ , and parameters  $\sigma_w$ ,  $C_{wT}$ ,  $C_{wq}$ , and  $C_{Tq}$ , the statistic distributions of the initial conditions are determined.

In the parameterization,  $w$  is discretized into  $N_1$  bins between 0 and  $\alpha \sigma_w$  (we use a  $\alpha$  of 3, and the truncated tail is sufficiently small):

$$w_i = \frac{i \alpha \sigma_w}{N_1}, \quad i = 1, \dots, N_1, \quad (12)$$

$$s_i = \frac{\alpha}{\sqrt{2\pi} N_1} \exp \left[ -\frac{(i\alpha)^2}{2N_1^2} \right]. \quad (13)$$

We can also view  $s_i$  as the fractional area occupied by the parcels belonging to the  $i$ th bin. The mass of parcels in the  $i$ th bin that cross the lowest model level above the surface over area  $A$  during  $\Delta t$  is

$$M_i = \rho \times \text{velocity} \times \text{area} \times \text{time} = \rho w_i s_i A \Delta t. \quad (14)$$

We further divide the air mass of each bin into  $N_2$  parcels equally. So the total number of parcels released is  $N_1 \times N_2$  and the mass of each parcel is

$$m_i = \frac{\rho s_i w_i A \Delta t}{N_2}. \quad (15)$$

The reason to divide each bin is because entrainment in this parameterization is a stochastic process. It requires the number of parcels to be large enough to ensure statistical stability. We will find later that the factor  $A \Delta t$  is cancelled in the calculation of convective tendencies.

In our method, because  $s_i$  decays exponentially as  $i^2$  increases, the total mass of parcels with large  $w$  is much smaller than that of parcels with smaller  $w$ . By using the same  $N_2$  for all vertical velocity bins, the implied mass per parcel is much smaller for the high  $w$  bins. One could carefully divide the  $i$ th bin into  $N_{2,i}$  parcels so that each parcel has a mass that is close to the mass of air blobs in the real atmosphere (or the LES). However, in that case we will find the number of low  $w$  parcels to be much larger than the number of high  $w$  parcels, and most of the computational resources will be spent on the low  $w$  parcels, which are less important in the convective mass flux calculation, instead of the high  $w$  parcels, which will be underrepresented given computational constraints. Furthermore, the implied mass per parcel is inconsequential in our scheme because drag force is ignored in this parameterization, so that the size of a parcel does not affect its evolution and the outputs of the parameterization. In other words, we set all  $N_{2,i}$  to the same value for computational economy and do not suggest that there is certain relationship between the size of the parcel and its vertical velocity.

With the initial statistical distributions in place, parcels are drawn randomly from this distribution and released from the lowest model layer. These parcels will rise, mix with the environment, oscillate around their neutral buoyancy level, and eventually come to rest. The evolution history of the parcels is solved by integrating the prognostic equations of parcel properties, with the entrainment processes specified as in section 2a and in Romps and Kuang (2010a,b). Because the mixing processes in the subcloud layer are different from those in the cloud layer, a different set of entrainment parameters  $[\lambda, \sigma]$  are used in the subcloud layers and tuned to give satisfactory results. Since we focus on shallow convection, precipitation and ice processes are turned off.

The temperature and moisture fluxes affected by the parcels are used to estimate the convective heating and moistening tendencies. Let the environmental soundings  $(\theta_{l,\text{en}}, q_{l,\text{en}})$  be specified on discrete levels  $Z$ . (We choose  $\theta_l$  as the prognostic temperature variable.) The fluxes are defined on half levels  $Z_h$ . The transports (fluxes times area times time) carried by these parcels across a certain level can easily be obtained by summing over all parcels that cross this level:

$$\text{mass transports} = \sum m_k, \quad (16)$$

$$\theta_l \text{ transports} = \sum m_k \theta_{l,k}, \quad (17)$$

$$q_l \text{ transports} = \sum m_k q_{l,k}, \quad (18)$$

where  $k$  is the index of parcels that cross this level over a time interval  $\Delta t$ . For parcels crossing this level from above, their transports should be marked as negative.

When the parcels rise, the environmental air subsides to compensate for the mass transport by these parcels and ensures that there is no net mass accumulation. The subsiding air also transports heat and moisture:

$$\text{compensating mass transports} = -\sum m_k, \quad (19)$$

$$\text{compensating } \theta_l \text{ transports} = -\sum m_k \theta_{l,\text{dn}}, \quad (20)$$

$$\text{compensating } q_l \text{ transports} = -\sum m_k q_{l,\text{dn}}, \quad (21)$$

where  $\theta_{l,\text{dn}}$  and  $q_{l,\text{dn}}$  are the mean  $\theta_l$  and  $q_l$  for the compensating subsidence. Here we approximate the properties of the compensating subsidence by its mean values, thus neglecting transport due to variations within the compensating subsidence. This is a good approximation for the cloud layer (Siebesma and Cuijpers 1995) but is less accurate in the subcloud layer. Here  $\theta_{l,\text{dn}}$  is estimated as

$$\theta_{l,\text{dn}} = \frac{\theta_{l,\text{en}} - \sum s_k \theta_{l,k}}{1 - \sum s_k}, \quad (22)$$

and the same for  $q_{l,\text{dn}}$ . The fractional area  $s_k$  occupied by a parcel at an interface averaged over a unit time is

$$s_k = \frac{m_k}{\rho_k w_k A \Delta t}. \quad (23)$$

The total fractional area occupied by convective updrafts  $\sum s_k$  is significant in the subcloud layer and negligible in the cloud layer.

The convective heating and moistening tendencies are the vertical convergence of the net fluxes (sum of the parcel transports and the compensating transports, then normalized by  $A$  and  $\Delta t$ ):

$$\bar{\rho} \frac{\partial \theta_{l,\text{en}}}{\partial t} = -\frac{\partial \left[ \sum (m_k \theta_{l,k}) - \sum m_k \theta_{l,\text{dn}} \right]}{\partial z} \frac{1}{A \Delta t}, \quad (24)$$

$$\bar{\rho} \frac{\partial q_{l,\text{en}}}{\partial t} = -\frac{\partial \left[ \sum (m_k q_{l,k}) - \sum m_k q_{l,\text{dn}} \right]}{\partial z} \frac{1}{A \Delta t}. \quad (25)$$

From Eq. (15), we see that  $A$  and  $\Delta t$  will be cancelled out in Eqs. (24) and (25).

## b. The BOMEX run

We test the parameterization by running it in the BOMEX setting. The BOMEX initial soundings, large-scale forcing, and surface fluxes for the parameterization run are the same as in Siebesma and Cuijpers (1995). The vertical levels are from 80 to 3000 m with a spacing of 160 m. The environmental soundings are adjusted every  $\Delta t = 60$  s. The time integration scheme of Eqs. (24) and (25) is forward Euler. The fluxes (17) and (18) are calculated by sampling the properties of parcels at half levels. When calculating the compensating fluxes (20) and (21), the minimum modulus (minmod) flux limiter scheme (Durrant 1999) is used. The parameterization is integrated for 3 h.

Parameters for the surface initial conditions are  $C_{wT} = 0.58$ ,  $C_{qT} = 0.55$  [the same as in Cheinet (2003) and Stull (1988), although we use  $T$  instead of  $\theta_v$  in these correlation coefficients], and  $C_{wq} = 0.63$  (which comes from our LES diagnoses). We find that the parameterization results are not sensitive to those correlation coefficients over a large range. By setting  $N_1 = 15$ ,  $N_2 = 10$ , the output is already statistically steady. Runs with much larger  $N_1$  and  $N_2$  do not alter the results.

We use the same entrainment parameters [ $\lambda = 125$  m,  $\sigma = 0.32$ ] as described in section 2. We find that the parameterization gives nearly equally good performance for large ranges of  $[\lambda, \sigma]$  along the bottom of the valley of the objective function in Fig. 7 of Romps and Kuang (2010b). Closer to the constant entrainment limit, however, the results degrade, and the intracloud variations (see later in Fig. 14) are severely underestimated. The cloud base is around 600 m in the BOMEX case. For this first study, the subcloud layer entrainment parameters are specified as  $[\lambda_{\text{sbc}}, \sigma_{\text{sbc}}] = [30 \text{ m}, 0.06]$ , yielding fairly good results. In the future, efforts are needed to better constrain  $[\lambda_{\text{sbc}}, \sigma_{\text{sbc}}]$ .

The initial sounding and the sounding after 3 h are shown in Figs. 12a,b. Although there are some drifts in the mean state, the convective tendency generally balances the large-scale forcing. The fluxes given by the parameterization (Figs. 12c,d) are broadly similar to the LES results (Siebesma and Cuijpers 1995; Cheinet 2004), except that our parameterization overpredicts both the negative  $\theta_l$  flux and the positive  $q_l$  flux near 1300 m.

We now sample the mean properties of “active cloudy air” for both the LES and the parameterization. Results using two definitions of active cloudy air are shown: one is cloudy updraft air as in section 3 (parcels/grids with  $q_l > 10^{-5} \text{ kg kg}^{-1}$  and  $w > 0.5 \text{ m s}^{-1}$ ) and the other is cloud core with the same definition as in Cheinet (2004) (parcels/grids with  $q_l > 10^{-5} \text{ kg kg}^{-1}$ ,  $w > 0 \text{ m s}^{-1}$ , and positively buoyant). The results show that the parameterization generally reproduces the results of LES with

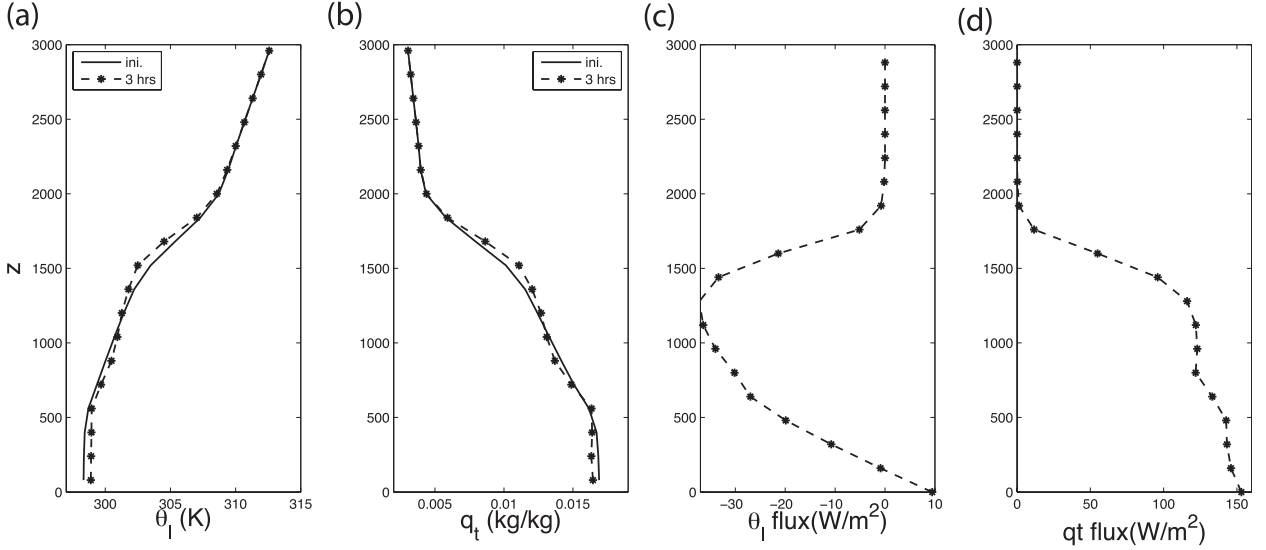


FIG. 12. (a) The initial  $\theta_l$  profile (solid) and the profile after a 3-h parameterization run (dot-dashed). (b) As in (a), but for the  $q_t$  profile. (c) The parameterization-generated  $\theta_l$  flux averaged between 1.5 and 3 h of the parameterization run. (d) As in (c), but for the  $q_t$  flux.

both definitions (Fig. 13). The exception is the cloud core  $w$  in the inversion. We have also examined the mean properties of cloudy air (saturated), or active cloud core with other definitions; the results all show agreement between the LES and the parameterization except for  $w$  in the inversion.

Besides the mean values of these properties, the standard variations are also examined (Fig. 14). Once again, except for layers that are in the inversion (above

1500 m), the parameterization and the LES results match well. The discrepancy in  $w$  between the LES and the parameterization in the inversion layer is not fully understood and requires further investigation. One possible reason for the decrease in the LES simulated  $w$  could be enhanced wave drag. As parcels penetrate into the inversion layer, a region of strong stratification and thus higher buoyancy frequency, they can become more effective in exciting gravity waves and therefore become

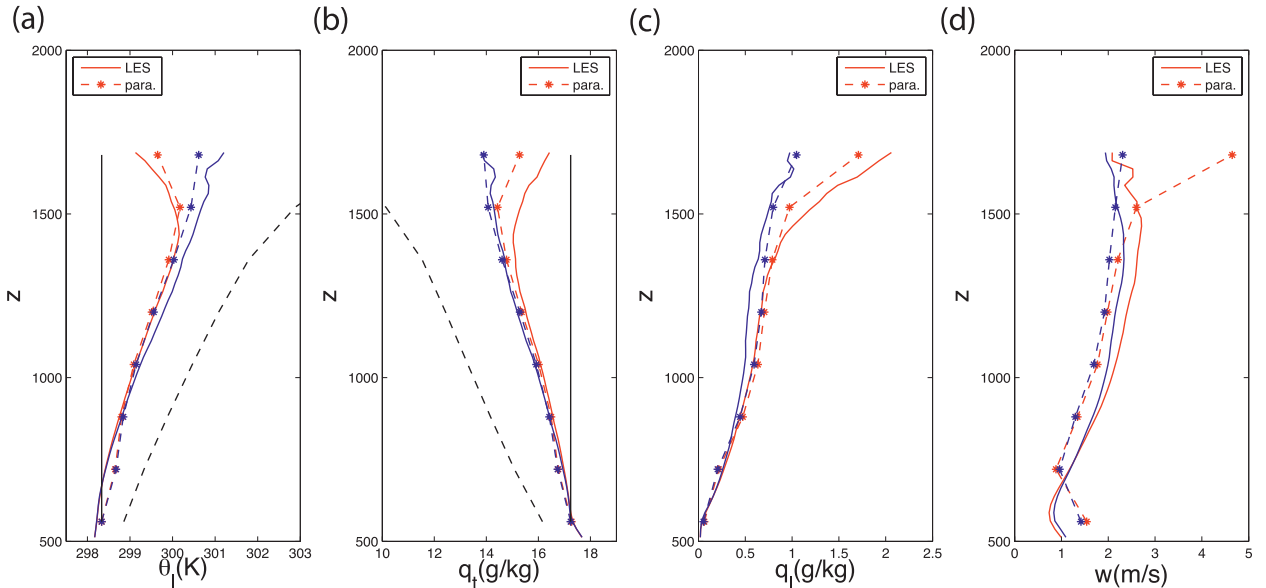


FIG. 13. The mass flux weighted properties [(a)  $\theta_l$ , (b)  $q_t$ , (c)  $q_b$ , and (d)  $w$ ] of cloudy updrafts. Solid lines are LES results and dot-dashed lines are results from the parameterization. The blue curves are for cloudy updrafts, while the red curves are for the cloud cores. See text for definition. In (a) and (b), the black dashed lines are the environmental profiles and the black solid lines are the adiabatic profiles from the cloud base.

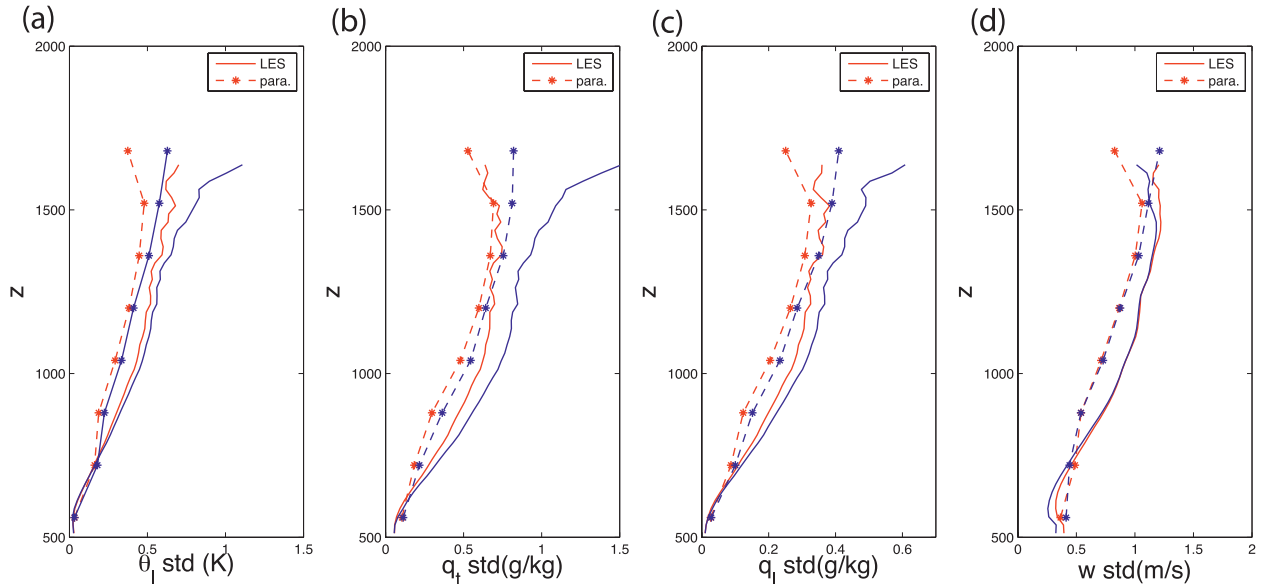


FIG. 14. The standard deviation among modeled cloudy updrafts for (a)  $\theta_1$ , (b)  $q_1$ , (c)  $q_l$ , and (d)  $w$ . Solid lines are LES results and dot-dashed lines are results from our parameterization. The blue curves are for cloudy updrafts; the red curves are for the cloud cores.

subject to enhanced gravity wave drag. Such processes are absent in the current parameterization. However, we note that Warren (1960) provided wave drag solutions that we can incorporate into our parameterization in the future.

### c. Response of the parameterization to temperature and moisture perturbations

Another important aspect of the parameterization is to capture the response of convection to changes in the large-scale environment. To this end, we have computed the linear response functions (hereafter as the LRF matrix) of this parameterization to a full set of temperature and moisture perturbations. The LRF matrix of the parameterization is calculated by simply adding, one at a time, temperature/moisture anomalies in each layer of the mean sounding. The anomalous heating and moistening tendencies from the parameterization form the LRF matrix. A comparison of the full LRF matrices from the parameterization and from the LES will be reported in a future paper. Here we shall only discuss the three perturbed cases (T987, T1262, Q987) described in section 3.

With the LRF matrix  $\mathbf{M}$ , we can compute the evolution of any perturbations by integrating the equation

$$\frac{d\mathbf{X}}{dt} = \mathbf{M}\mathbf{X}, \quad (26)$$

where  $\mathbf{X}$  is the state vector (temperature and moisture profile) (Kuang 2010). The time evolution of the sounding anomalies for the T987, T1262, and Q987 cases is shown in Fig. 15 and should be compared with LES

results shown in Figs. 1, 7, and 9. Note that results in Fig. 15 are for an integration over 3 h. The agreement is quite good in terms of both the pattern and the magnitudes of the responses. The warming seen in the parameterization in response to the moisture perturbation, however, appears stronger than that in the LES.

## 5. Conclusions and discussion

In this paper, the responses of a shallow cumulus ensemble to large-scale temperature and moisture perturbations are investigated using an LES and a stochastic parcel model. We have further introduced a parameterization of shallow cumulus convection (including subcloud layer turbulence) based on the stochastic parcel model.

The main findings are as follows:

- 1) The SPM in general reproduces the LES responses to large-scale temperature and moisture perturbations, not only in terms of the domain-mean heating and moistening tendencies but also in terms of changes in the statistics of the cloudy updrafts. The stochastic entrainment scheme in the SPM is key for the SPM to match the LES results. It suggests that the stochastic entrainment approach is a good way of representing the mixing process in simple models.
- 2) There are, however, some discrepancies in the  $w$  field between the SPM and LES responses, suggesting that the treatment of momentum evolution in the SPM might be overly simplistic.

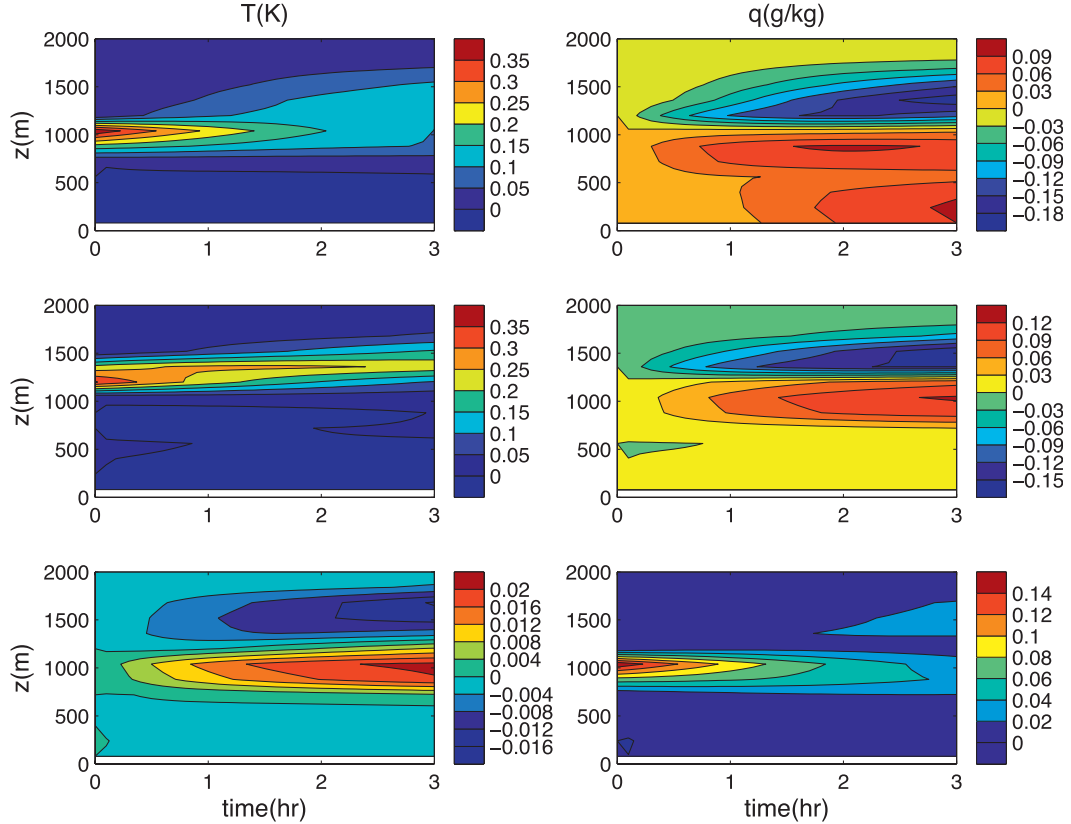


FIG. 15. Evolutions of (left) temperature and (right) moisture anomalies after the initial perturbation is introduced as simulated using the linear response functions of the parameterization for the (top) T987, (middle) T1262, and (bottom) Q987 cases.

- 3) A positive temperature perturbation to the environmental sounding forms a buoyancy barrier that inhibits cloudy updrafts that have lower initial  $\theta_e$  or entrain heavily.
- 4) For parcels that have the same amount of entrainment, the height at which parcels entrain is important in deciding their fate. Parcels entraining at higher altitudes are more likely to survive the buoyancy barrier and vice versa.
- 5) Convective heating responses to moisture perturbation above the cloud base are quite small for a shallow cumulus regime such as BOMEX.
- 6) A parameterization based on the stochastic parcel model gives promising results in terms of both the simulated mean state and the variation and the simulated responses to temperature and moisture perturbations.

We argue that an important advantage of the SPM and the parameterization based on it is that they explicitly include the inhomogeneity of cloudy air associated with the stochastic mixing process. Although other ensemble plume/parcel models also contain some inhomogeneity of cloudy air at the same height, the

inhomogeneity is only introduced through variations in the cloud-base conditions (e.g., Neggers and Siebesma 2002). The present approach includes the variations introduced by the stochastic nature of mixing, which was shown to be the main cause of inhomogeneity in cloudy air (Romps and Kuang 2010b). Capturing this inhomogeneity is important in order to better simulate microphysics and chemistry beyond the goal of simulating the heating and moistening tendencies. Compared to the assumed PDF approach (e.g., Lappen and Randall 2001; Larson et al. 2002; Golaz et al. 2002), the present approach may be viewed as a Monte Carlo version of the PDF approach; while it is somewhat more expensive, it can be more general and versatile in dealing with different PDFs. We note that cost saving with this parameterization may be achieved using the approach of Pincus et al. (2003), where one subsamples the PDFs at each time step but builds up sufficient sampling over many time steps of the model integration.

Certain treatments in the present parameterization are chosen for simplicity and could and should be improved in the future. For example, the current neglect of momentum drag on the parcels, including the lack of



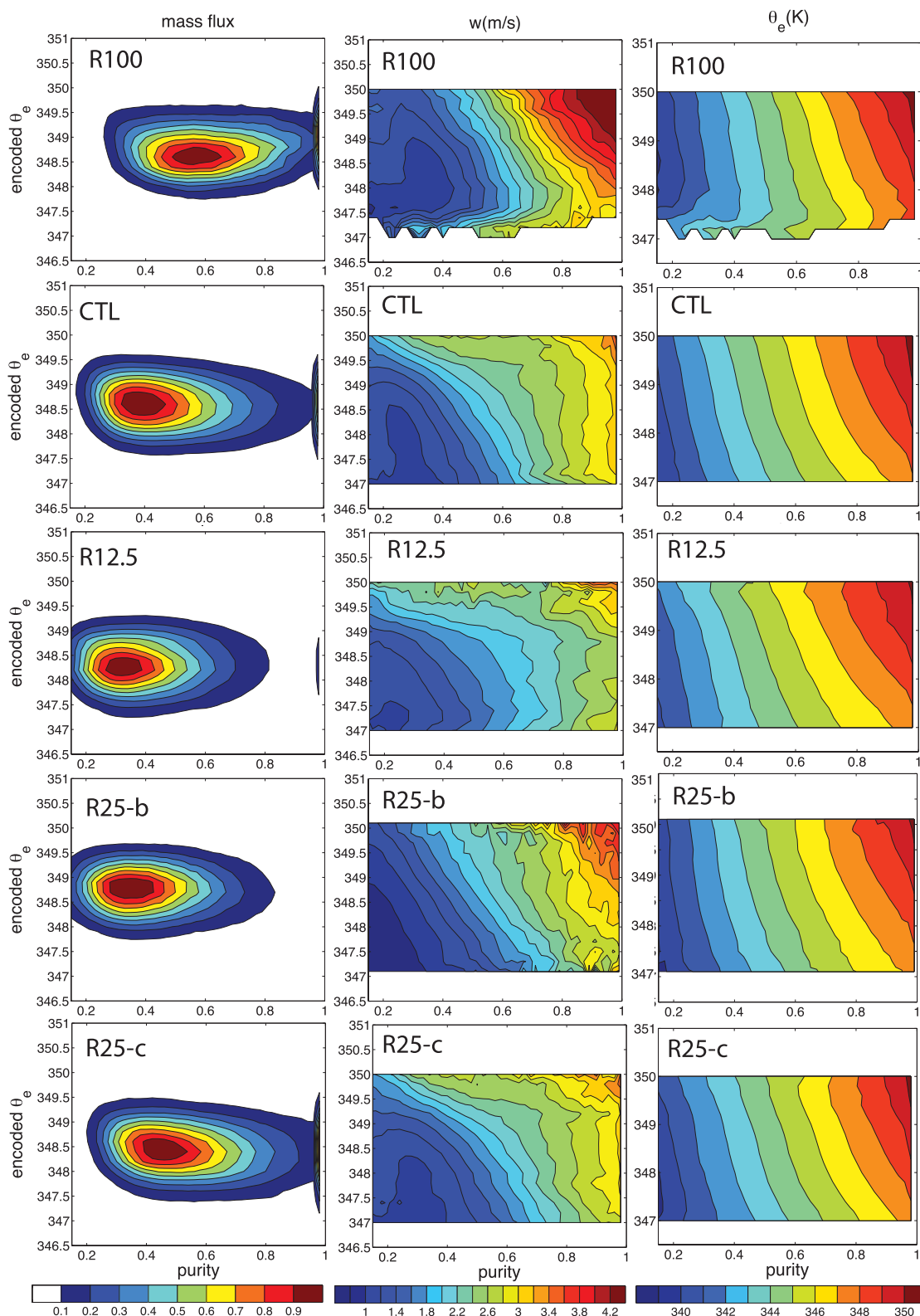


FIG. A1. Cloud updraft statistics of (left) mass flux, (middle)  $w$ , and (right)  $\theta_e$  with different LES settings as listed in Table 1. The simulation names are labeled on the top-left corner of each panel. The panels for the CTL simulations are as in Figs. 2a–c and are included here to facilitate comparison.

wave drag, is clearly unrealistic. Notwithstanding the need to balance simplicity and realism, effects of gravity wave drag as described in Warren (1960) should be explored. The lack of interparcel interaction is also an idealization based on a limiting scenario, bulk plume being the opposite extreme of instant interparcel homogenization. In-cloud mixing of parcels and/or momentum exchanges without actual mixing of parcels could be added in the spirit of Krueger et al. (1997). We have limited ourselves to shallow nonprecipitation cumuli in the current parameterization and have neglected precipitation processes. How to extend the current model to include the additional processes brought about by precipitation so that it can serve as a unified parameterization for both shallow and deep convection is a research question for future studies.

**Acknowledgments.** We thank David Romps for help and discussions with the DAM and SPM models at the initial stage of the project, Steve Krueger for helpful comments, and Steve Sherwood and Brian Mapes for valuable reviews that helped to improve the paper. This research was partially supported by the Office of Biological and Environmental Research of the U.S. Department of Energy under Grant DE-FG02-08ER64556 as part of the Atmospheric Radiation Measurement Program and NSF Grants ATM-0754332 and AGS-1062016. The Harvard Odyssey cluster provided much of the computing resources for this study.

## APPENDIX

### Sensitivity Tests of the LES

In this appendix, we explore the sensitivity of the results in Fig. 2 to model resolution and to the size of the protective halo around cloudy updrafts used in tracer encoding. The list of sensitivity experiments is given in Table 1 and the results are shown in Fig. A1.

To test the resolution dependence of the LES, in addition to the  $dx = dy = dz = 25$  m case (the CTL run), we have made experiments with  $dx = dy = 100$  m and  $dz = 50$  m (the R100 run), and with  $dx = dy = dz = 12.5$  m (the R12.5 run). In the R100 run, the  $w$  contours are oriented from upper left to lower right. In the R12.5 run, on the other hand, the  $w$  contours are more vertical in regions with high purity and more horizontal in regions with high encoded  $\theta_e$ , similar to what was seen in the control experiment, indicating that such behaviors are robust for high-resolution runs. These results are also consistent with our hypothesis in section 3a that the different behaviors in  $w$  and thermodynamic variables such as  $\theta_e$  are due to intracloud variations; the higher-resolution simulations better

resolve the clouds and therefore have more intracloud variations.

To further test the role of intracloud variations, we average the output from the control experiment, which has  $dx = dy = dz = 25$  m to a grid of  $dx = dy = 100$  m and  $dz = 50$  m before computing the statistics. The results, shown in the fourth row of Fig. A1 and labeled as R25-b, are similar to those from the R100 run, with  $w$  and  $\theta_e$  exhibiting similar behaviors. This further supports the notion that the different behaviors in  $w$  and thermodynamic variables such as  $\theta_e$  are due to intracloud variations.

We have also tested the sensitivity to an uncertain parameter in the tracer encoding procedure. As described in section 2a, with the tracer-encoding technique, the purity and equivalent potential temperature tracers are set to zero at every time step above the tracer release level except in the vicinity of cloudy updrafts, which is defined by a protective halo surrounding the cloudy updrafts. The size of this protective halo should be large enough to preserve tracer values at grid points that, while not qualified as cloudy updrafts themselves, are part of the circulation immediately associated with the cloudy updrafts. The size of this protective halo should also be small enough so that air not associated with the ongoing cloudy updrafts (i.e., the environmental air) has zero tracer values. The precise value of the halo size is uncertain, which is a limitation of the tracer-encoding technique. For the control experiments presented in Figs. 2a–c, the halo size is three grid points (or 75 m). In experiment R25-c, we set the halo size to 300 m. The main effect is a small shift in the mass flux distribution toward higher purity as expected from the wider protective halo. The salient features of the  $w$  distribution remain unchanged.

## REFERENCES

- Arakawa, A., and W. H. Schubert, 1974: Interaction of a cumulus cloud ensemble with the large-scale environment, Part I. *J. Atmos. Sci.*, **31**, 674–701.
- Bechtold, P., E. Bazile, F. Guichard, P. Mascart, and E. Richard, 2001: A mass-flux convection scheme for regional and global models. *Quart. J. Roy. Meteor. Soc.*, **127**, 869–886.
- Bony, S., and J.-L. Dufresne, 2005: Marine boundary layer clouds at the heart of tropical cloud feedback uncertainties in climate models. *Geophys. Res. Lett.*, **32**, L20806, doi:10.1029/2005GL023851.
- , —, H. Le Treut, J.-J. Morcrette, and C. Senior, 2004: On dynamic and thermodynamic components of cloud changes. *Climate Dyn.*, **22**, 71–86.
- Bretherton, C. S., J. R. McCaa, and H. Grenier, 2004: A new parameterization for shallow cumulus convection and its application to marine subtropical cloud-topped boundary layers. Part I: Description and 1D results. *Mon. Wea. Rev.*, **132**, 864–882.

- Cheinet, S., 2003: A multiple mass flux parameterization for the surface-generated convection. Part I: Dry plumes. *J. Atmos. Sci.*, **60**, 2313–2327.
- , 2004: A multiple mass flux parameterization for the surface-generated convection. Part II: Cloudy cores. *J. Atmos. Sci.*, **61**, 1093–1113.
- Durrán, D. R., 1999: *Numerical Methods for Wave Equations in Geophysical Fluid Dynamics*. Springer, 267 pp.
- Emanuel, K. A., 1991: A scheme for representing cumulus convection in large-scale models. *J. Atmos. Sci.*, **48**, 2313–2329.
- Golaz, J.-C., V. E. Larson, and W. R. Cotton, 2002: A PDF-based model for boundary layer clouds. Part I: Method and model description. *J. Atmos. Sci.*, **59**, 3540–3551.
- Kain, J. S., and M. Fritsch, 1990: A one-dimensional entraining/detraining plume model and its application in convective parameterization. *J. Atmos. Sci.*, **47**, 2784–2802.
- Krueger, S. K., C.-W. Su, and P. A. McMurtry, 1997: Modeling entrainment and finescale mixing in cumulus clouds. *J. Atmos. Sci.*, **54**, 2697–2712.
- Kuang, Z., 2010: Linear response functions of a cumulus ensemble to temperature and moisture perturbations and implication to the dynamics of convectively coupled waves. *J. Atmos. Sci.*, **67**, 941–962.
- Lappen, C.-L., and D. A. Randall, 2001: Toward a unified parameterization of the boundary layer and moist convection. Part I: A new type of mass-flux model. *J. Atmos. Sci.*, **58**, 2021–2036.
- Larson, V. E., J.-C. Golaz, and W. R. Cotton, 2002: Small-scale and mesoscale variability in cloudy boundary layers: Joint probability density functions. *J. Atmos. Sci.*, **59**, 3519–3539.
- Mapes, B. E., 2004: Sensitivities of cumulus-ensemble rainfall in a cloud-resolving model with parameterized large-scale dynamics. *J. Atmos. Sci.*, **61**, 2308–2317.
- Neggers, R. A. J., and A. P. Siebesma, 2002: A multiparcel model for shallow cumulus convection. *J. Atmos. Sci.*, **59**, 1655–1668.
- Pincus, R., H. W. Barker, and J. J. Morcrette, 2003: A fast, flexible, approximate technique for computing radiative transfer in inhomogeneous cloud fields. *J. Geophys. Res.*, **108**, 4376, doi:10.1029/2002JD003322.
- Raymond, D. J., and A. M. Blyth, 1986: A stochastic mixing model for nonprecipitating cumulus clouds. *J. Atmos. Sci.*, **43**, 2708–2718.
- , and M. J. Herman, 2011: Convective quasi-equilibrium reconsidered. *J. Adv. Model. Earth Syst.*, **3** (14), M08003, doi:10.1029/2011MS000079.
- Romps, D. M., 2008: The dry-entropy budget of a moist atmosphere. *J. Atmos. Sci.*, **65**, 3779–3799.
- , and Z. Kuang, 2010a: Do undiluted convective plumes exist in the upper tropical troposphere? *J. Atmos. Sci.*, **67**, 468–484.
- , and —, 2010b: Nature versus nurture in shallow convection. *J. Atmos. Sci.*, **67**, 1655–1666.
- Sherwood, S., M. Colin, and F. Robinson, 2010: A revised conceptual model of cumulus clouds as thermal vortices. *Eos, Trans. Amer. Geophys. Union*, **91** (Fall Meeting Suppl.), Abstract A24C-04.
- Siebesma, A. P., and J. W. M. Cuijpers, 1995: Evaluation of parametric assumptions for shallow cumulus convection. *J. Atmos. Sci.*, **52**, 650–666.
- Simpson, J., 1971: On cumulus entrainment and one-dimensional models. *J. Atmos. Sci.*, **28**, 449–455.
- Stull, R. B., 1988: *An Introduction to Boundary Layer Meteorology*. Kluwer Academic, 670 pp.
- Tiedtke, M., 1989: A comprehensive mass flux scheme for cumulus parameterization in large-scale models. *Mon. Wea. Rev.*, **117**, 1779–1800.
- Tulich, S. N., and B. E. Mapes, 2010: Transient environmental sensitivities of explicitly simulated tropical convection. *J. Atmos. Sci.*, **67**, 923–940.
- Warren, F. W. G., 1960: Wave resistance to vertical motion in a stratified fluid. *J. Fluid Mech.*, **7**, 209–229.
- Yanai, M., S. Esbensen, and J.-H. Chu, 1973: Determination of bulk properties of tropical cloud clusters from large-scale heat and moisture budgets. *J. Atmos. Sci.*, **30**, 611–627.